metals

MDPI

Review

Mechanical and Wear Properties of Additive Manufactured Metal Matrix Composites: A Review

Haris Farooq Kiani, Nan Xiao, Zan Li * and Shaofan Ge *

State Key Laboratory of Metal Matrix Composites, Shanghai Jiao Tong University, Shanghai 200240, China
* Correspondence: njulizan@sjtu.edu.cn (Z.L.); geshaofan@sjtu.edu.cn (S.G.)

Abstract

In critical sectors such as energy, transportation, and high-end manufacturing, components must endure simultaneous exposure to high temperatures, heavy loads, and severe wear, necessitating materials with balanced strength, toughness, and durability. Metal matrix composites (MMCs), enhanced with ceramic reinforcements, offer a promising solution to these multifaceted demands. While conventional techniques like casting and powder metallurgy often struggle with limited design freedom and uniform reinforcement distribution, additive manufacturing (AM) enables the production of complex, graded components with tailored microstructures and unlocks new possibilities for materials operating under extreme service conditions. This review systematically examines recent advances in AM-processed MMCs—focusing on aluminum-, titanium-, nickel-, and steel-based systems—for applications in coupled extreme environments. It provides a detailed analysis of their high-temperature mechanical performance and wear resistance, emphasizing the roles of reinforcement selection, microstructural design, and AM processing parameters in governing key properties. Furthermore, the underlying strengthening and wear mechanisms are discussed, along with current challenges and future opportunities. This work aims to serve as a foundational reference for the development of next-generation AM MMCs tailored for high-performance engineering applications.

Keywords: additive manufacturing; metal matrix composites; extreme service conditions; mechanical properties; wear resistance

1. Introduction

In the ongoing evolution of advanced high-end equipment, the service environment for core hot-section components has become increasingly severe, entering an era characterized by the deep coupling of multiple extreme conditions: high temperature, heavy loads, and severe wear [1–5]. For instance, turbine blades and tenons in aero-engines endure not only prolonged exposure to high-temperature gas wash exceeding 1000 °C and massive centrifugal stress but also suffer from stress-concentrating fretting wear at their connections [6]. Similarly, the thrust chamber liners of liquid rocket engines must maintain structural integrity under extreme temperatures of several thousand degrees Celsius, pressures of tens of megapascals, and intense thermal shock cycles, while simultaneously resisting chemical corrosion and particle erosion from high-temperature combustion gases [7]. This "complex extreme service environment," integrating high heat, high load, and high wear, poses an unprecedented ultimate challenge to material performance. A single performance metric is no longer sufficient; materials must seek an optimal balance between interrelated and often contradictory properties, such as high strength versus high toughness, and surface

Check for updates

Academic Editors: Wislei Riuper Osório and Ausdinir Danilo Bortolozo

Received: 31 December 2025
Revised: 6 February 2026
Accepted: 8 February 2026
Published: 26 February 2026

Copyright: © 2026 by the authors. Licensee MDPI, Basel, Switzerland. This article is an open access article distributed under the terms and conditions of the Creative Commons Attribution (CC BY) license.

hardness versus overall fracture resistance. Any deficiency in one aspect can become the origin of component failure.

Traditional homogeneous metallic materials (e.g., nickel-based superalloys, titanium alloys) or metal matrix composites (MMCs) fabricated via conventional methods like casting, forging, powder metallurgy [8], mechanical alloying [9], and electrodeposition technique [10] are increasingly inadequate in addressing these multi-dimensional challenges. Their limitations are primarily reflected in the following aspects: Firstly, the room for performance enhancement is constrained, as the compositional and microstructural optimization of traditional alloys is approaching its limits. Secondly, manufacturing process constraints make it difficult to achieve the integral forming of complex components possessing an optimal wear-resistant surface combined with a tough matrix. Issues such as reinforcement phase segregation and uncontrolled interfacial reactions remain prominent. Thirdly, insufficient design freedom hinders the efficient manufacturing of complex geometries that integrate lightweight structures, internal cooling channels, and functional gradients. These bottlenecks severely restrict the development of a new generation of equipment with higher efficiency and longer service life.

Additive manufacturing (AM) technologies, particularly laser powder bed fusion (LPBF) and directed energy deposition (DED), provide a revolutionary solution to break through these bottlenecks [2,11–13]. They not only enable "freeform fabrication" from three-dimensional models to final parts, unlocking unprecedented geometric design capabilities, but more importantly, bring a paradigm shift to the design and fabrication of MMCs. Their core advantages lie in the following. Precise microstructural control: leveraging extremely high cooling rates (up to 10^6 K/s) to achieve ultrafine grains, supersaturated solid solutions, and metastable phases, while effectively inhibiting the coarsening of reinforcement phases [14]. Uniform and novel reinforcement distribution: through methods such as powder premixing, in situ reactions, or multi-material synchronous feeding, a highly dispersed distribution of nano- to micro-scale reinforcement phases within the matrix can be realized, forming clean and strongly bonded interfaces [15]. Spatial customization of composition and performance: enabling the integrated fabrication of functionally graded materials, allowing different regions of a component to be optimized for specific functions such as thermal management, load-bearing, or wear resistance [16,17]. Additionally, AM offers distinct economic and manufacturing advantages: it is cost-effective for small-batch, customized production by eliminating the need for expensive molds and tooling; it achieves high material utilization through near-net-shape forming, minimizing waste and enabling lightweight design; and it facilitates integrated manufacturing of complex geometries, reducing assembly steps and shortening production lead times. These characteristics empower additively manufactured metal matrix composites (AM MMCs) to potentially achieve the synergistic unity of high strength, high toughness, high wear resistance, and long service life in complex service environments.

In light of this, this review aims to systematically summarize the latest research progress in AM MMCs designed for high-temperature, high-load, and high-wear complex extreme service conditions. This article will first analyze the multi-factor coupling characteristics of such conditions and their comprehensive demands on materials. Subsequently, following a material-system framework, it will delve into the research status of additively manufactured aluminum-based, titanium-based, nickel-based, and steel-based composites in separate sections. The focus will center on the relationship of "Reinforcement Selection–Additive Manufacturing Process–Microstructural Architecture–High-Temperature Mechanical/Tribological Performance," analyzing their underlying strengthening and wear-resistance mechanisms (e.g., grain refinement, dislocation strengthening, load transfer effect, formation of oxidative tribolayers). Finally, the article will summarize current key

challenges (e.g., anisotropy, defect control, performance prediction) and provide an outlook on future research directions, including machine learning-assisted material and process design, multi-scale and lifecycle simulation, and next-generation composite material systems for even more extreme environments.

This review hopes to provide researchers and engineers engaged in advanced material design and additive manufacturing with a clear perspective to understand the performance evolution of materials under multi-factor coupled service conditions, thereby promoting the design and application of the next generation of high-performance, highly reliable MMCs. The following sections will begin by systematically examining the tensile properties of various AM MMCs at both room and elevated temperatures, elucidating their potential and mechanisms in addressing high-load and high-temperature environments.

2. Room and High-Temperature Tensile Properties of AM MMCs

Metals have a broad range of tensile characteristics that make them appropriate for various engineering and manufacturing applications. Tensile properties are one of the most important mechanical characteristics of additively manufactured materials. In MMCs, tensile properties are essential due to their prompt effect on the composite's strength/ductility to bear mechanical stresses, defining its suitability for application in various specific fields. The incorporation of reinforcements, such as fibers, whiskers, or ceramic particles, helps to strengthen the matrix by preventing dislocation motion and bearing load to improve overall tensile strength, but may render local stress concentration to induce lower ductility [18]. This might be particularly true for AM metal composites due to the presence of defects such as porosity and cracks, which further reduce tensile ductility. This is an "Achilles' heel" of the AM metal composites, thereby requiring a deliberate design of composite microstructures. Moreover, at elevated temperatures, the stress level seems to progressively drop as plastic deformation increases, due to the softening processes of dynamic recovery (DRV) and dynamic recrystallization (DRX) of metal grains [19]. MMCs usually increase the recrystallization temperature, and the stability of grain boundary structures is also enhanced due to the pinning effect of reinforcements, improving high-temperature mechanical properties [20]. In general, some mechanisms responsible for the superior mechanical performance of AM composites deformed at high temperatures are the grain boundary pinning effect, dynamic recrystallization, and precipitation strengthening [21]. Here, the room and high-temperature tensile properties of different AM metal composites are firstly reviewed and discussed. The summary of tensile properties of AM MMCs is shown in Figure 1.

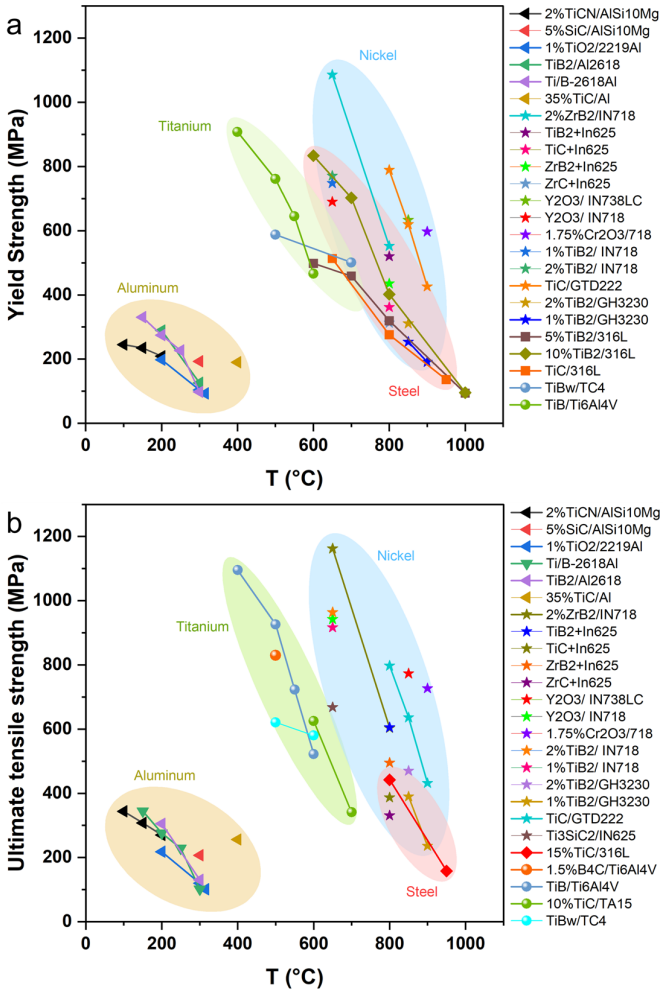


Figure 1. Tensile properties of additively manufactured metal matrix composites at elevated temperature. (**a**) Yield strength (YS), (**b**) ultimate tensile strength (UTS). (Table S1 in Supplementary Materials) [22–41].

2.1. Aluminum Matrix Composites (AMCs)

Aluminum matrix composites (AMCs) have distinctive characteristics, such as a low thermal expansion coefficient and high specific strength, which are useful in sectors like aerospace, automotive, and transportation where reducing weight is a critical design goal to improve fuel efficiency, performance, or payload capacity [42]. However, the typically slow solidification rate of conventional processing methods and limited wettability between the Al matrix and reinforcing phases sometimes led to weak interfacial bonding and unfavorable stress concentration. These disadvantages have significantly reduced the mechanical strength, which has limited their broad application [43]. Moreover, Al alloys usually experience a significant reduction in strength at elevated temperatures (as low as 200 °C). For example, the most widely used alloys in the AM field, the Al-Si alloys, severely lose strength at high temperatures (e.g., from 185 MPa at room temperature to 149 MPa at a temperature of 250 °C) [44]. Thermal softening also reduces the load-bearing capacity of reinforcements because of the reduced stress transfer from matrix to reinforcement [45]. Moreover, the precipitation of secondary phases (such as Al_2Cu and Mg_2Si, etc.) strengthens aluminum alloys, but these precipitates either dissolve or coarsen into the matrix at temperatures above 300 °C, further eliminating the strengthening effect. An elevated high-temperature usage of aluminum alloys requires a thermally stable microstructure and a strong interface [46]. Usually, elements with poor solubility and low diffusivity in aluminum matrix produce the coarsening-resistant intermetallic phases; this is because low

diffusivity, as well as poor solubility, establishes the kinetic and thermodynamic barrier for coarsening [47]. The strategies of incorporating ceramic particle reinforcements into metals/alloys to form a composite could naturally promote microstructure stability due to the pinning of grain boundaries with particles. Several B- and C-based reinforcements, such as TiB_2, TiC, TiCN, and SiC, have been attempted in Al alloys for better tensile properties, yet only a few attempts have been successful [48]. One of the most widely used reinforcements in conventional AMCs, SiC particles, however, may exhibit degraded tensile properties at both room and higher temperatures as a result of their decomposition at extremely high temperatures upon additive manufacturing [49]. The decomposition of SiC particles would cause surface turbulence, an unstable molten pool, and irregular scanning tracks [50]. Furthermore, a massive interfacial reaction between reinforcing particles and metals could greatly deteriorate the intrinsic properties of reinforcement and form brittle reaction products, reducing the tensile ductility at various operational temperatures [51].

Among all the probed AMCs, Ti-based reinforcing particles (e.g., TiB_2 and TiC) are generally applicable, likely due to their high melting point (above 2900 °C), strong interfacial bonding, and excellent thermal stability [52]. The advantages of the AM in modifying composite structures and the resultant mechanical properties can be embodied by the following two perspectives. (1) It promotes uniform dispersion of particles inside the matrix and prevents particulate agglomeration due to the complex melt pool dynamic under an extremely high cooling rate (>10^5 K/s) upon solidification [53]; and (2) fine grains can be developed at the melt pool boundaries as a result of the laser heat being absorbed and the fast solidification at heterogeneous nucleation sites, which endows an elimination of solidification cracks and isotropic mechanical properties [54]. Below, we focus on two of the most widely employed Ti-based reinforcing particles, TiC and TiB_2, which demonstrate generally higher tensile properties compared to other reinforcing particles in AM aluminium composites, as revealed in Figure 1a,b.

Remarkably, the Al matrix composite reinforced with 35% TiC particles exhibits a promising yield strength of 906 MPa, as shown in Figure 1a [28]. This extremely high yield strength was found to be associated with the grain refining effect of reinforcing particles. These particles first offer a high density of nucleation sites, which causes the liquid to solidify with finer grain sizes, and solidified aluminum grains are further stabilized due to the pinning effect by TiC nanoparticles, as shown in Figure 2a,b [55], giving rise to an average ultrafine grain size of 331 $\pm$ 95 nm, as illustrated in Figure 2c. Moreover, the nanoparticles on the powder surface were reported to efficiently absorb the laser beam, which allows the surface TiC nanoparticles to diffuse and disperse quickly into the center of the molten powders, exposing Al liquids for bonding into dense layers [56]. The rapid heating and cooling processes upon AM prevented TiC from chemically reacting with Al melts, contributing to a clean and robust interface structure [57]. Therefore, a combination of augmented nucleation sites, restricted grain growth, and a high cooling rate during AM gives rise to the extremely high YS and UTS in this kind of AM composites [58]. Similarly, Al-Cu-based alloys also showed enhanced yield and UTS behavior when incorporating the high-melting-point TiB_2 reinforcements, as shown in Figure 2a,b. The excellent thermodynamic compatibility between the originally introduced Ti and B allows them to pair up and form TiB_2 nuclei in the liquid phase, thus ensuring the stability of the reinforcing phase under a high-temperature environment upon AM (can reach up to 3000 °C for L-PBF process) [59]. The presence of TiB_2 nuclei also lowers the amount of undercooling needed for solidification, promoting the heterogeneous nucleation of Al grains [60]. Remarkably, the high-temperature tensile strength of the L-PBF TiB_2-reinforced Al-Cu-based alloys is higher than 130 MPa when deformed at 300 °C, as shown in Figure 1b, with an enhanced

tensile elongation to failure of 8.1%. A high strength retention is also demonstrated after prolonged thermal exposure up to 300 °C [61].

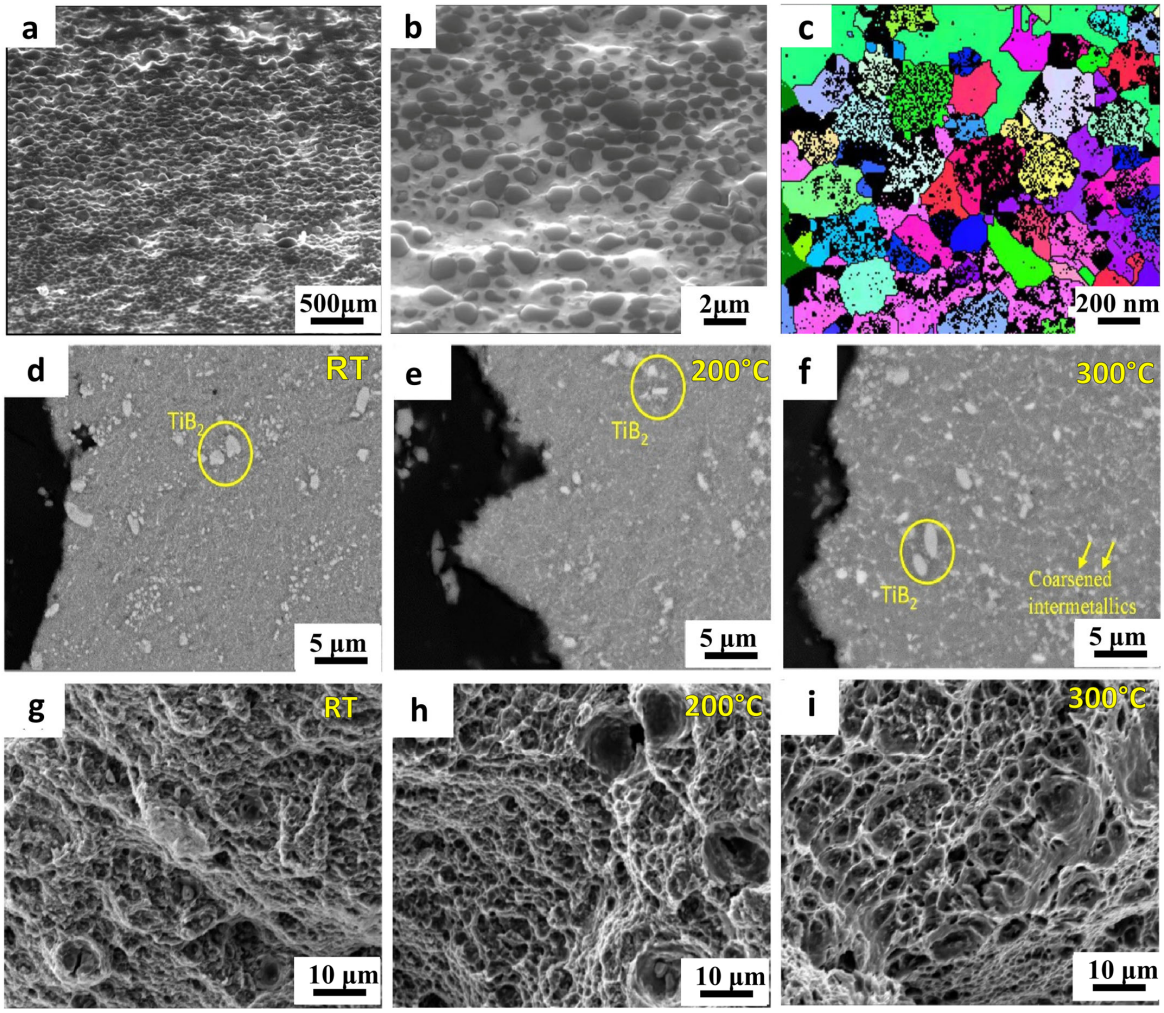


Figure 2. (**a**,**b**) The 52° tilted cross-sectional SEM images of laser-processed AMNC (35 vol.% TiC) were captured under different magnifications, showing that TiC nanoparticles are uniformly dispersed and distributed in aluminum. (**c**) The grain maps of laser-deposited AMNC (35 vol.% TiC). Reprinted from Ref. [28]. (**d**–**f**) Backscattered electron (BSE) images showing the microstructure near the fracture surfaces of the samples tested at RT, 200 °C, and 300 °C. (**g**–**i**) Typical fracture surfaces of the as-printed L-PBF TiB/Al2618 composite testing at RT, 200 °C, and 300 °C. Adapted with permission from Ref. [61]. 2023, Elsevier.

At elevated temperatures, the improved mechanical performances are mostly due to the combined effects of reinforcements and the coarsening-resistant compounds (e.g., Fe- and Ni-rich intermetallic phases in aluminium alloys), which offer the exceptional thermal stability of ultrafine microstructure and significant strengthening effects [29]. Moreover, the thermally stable intermetallic phases are refined as a result of the limited atomic diffusion and growth time due to the extremely rapid cooling of AM [62]. When tested at 200 °C, the TiB_2/Al2618 demonstrated very little loss in yield strength and tensile strength, which is related to the intermetallic phases that are mostly unaffected at this temperature, as shown in Figure 2d,e [61]. However, apparent coarsening of the intermetallic phases could occur at temperatures of 300 °C or above, leading to a considerably lower strength, as shown in Figure 2f [63]. It is known that higher temperatures cause thermal activation, which facilitates the propagation of dislocations and the grain boundary sliding

mechanism [64,65]. The incorporation of reinforcing particles near grain boundaries can efficiently "pin" the grain boundaries via the Zener pinning mechanism, inhibiting grain growth. The mechanism involves the balance between the driving force for grain growth (which seeks to reduce grain boundary energy) and the pinning force from reinforcing particles that prevent grain boundaries from moving [66]. This interplay results in the stabilization of grain size, maintaining the material's desired properties even at elevated temperatures. The limited particle size D_{lim} can be estimated as follows [67]:

$$D_{lim} = \frac{4\alpha r_p}{3f} \quad (1)$$

where the coefficient α ranges from 0.25 to 0.5, r_p is the mean particle radius, and f is the volume fraction of particles. Therefore, D_{lim} is calculated to range from 3.75 to 7.5 μm for the above AM TiB_2/Al2618 composite, which is relatively small and agrees well with the experiments.

In addition to the above two widely used particles, there are other types of reinforcements that could facilitate improved retained UTS and YS at high temperatures as well. As an example, TiCN offers great potential as a reinforcement in aluminum alloys because of its high strength (Vickers hardness value of 2500–3000) and high melting point (3050 °C) [68]. More importantly, it rarely produces any brittle reaction products in aluminum (such as Al_4C_3) during processing. As noted, the TiCN-reinforced AlSi10Mg composite made by L-PBF shows highly retained tensile yield strength and ultimate strength at a deformation temperature of 200 °C, as shown in Figure 1a,b [25].

Ductility is essential for AM composites at both room and high temperatures. The primary dislocation density and distributions are important variables that govern dislocation multiplication, storage, and annihilation of AM aluminum-based composites. Notably, the reinforcing particles exhibit a propensity to spread along grain boundaries due to the high interfacial energy, leading to a tendency for early crack initiation during tension deformation [69]. The AM TiB_2-reinforced aluminum composite shows dimple fracture features at room and high temperatures, and dimples become deeper and larger as the tensile temperature rises, suggesting a softer matrix and a preference for crack/void nucleation at interfaces, as shown in Figure 2g–i. The deformation incompatibility of the elastically deforming particles and the softened Al matrix is more prominent at high temperatures, facilitating crack nucleation at interfaces [70]. Moreover, the intergranular distribution of reinforcements in AM composites couples the stress concentration of phase and grain boundaries, which intensifies the fracture process and causes reduced ductility as compared to bare AM Al alloys at both room and high temperatures [71]. Hence, to improve the tensile ductility of AM aluminum composites, three ways could be harnessed: (1) The refinement of reinforcing particles. Nanoparticles have been extensively utilized in the conventionally fabricated AMCs, with the purpose of improving ductility. Nanoscale reinforcements can reduce the localization of stress at interfaces as well as the intrinsic fracture strength according to the principle of the Griffith criterion, thus retarding the nucleation of cracks [72,73]. They can also facilitate the formation of an equiaxed grain structure as nucleates and inhibit grain growth, which is beneficial for achieving homogeneous microstructures, such as a uniform second-phase distribution and fine-scale solidification grains [74]. These microstructures had been achieved in AM AMCs incorporated with nanoparticles. (2) The intragranular dispersion of reinforcing particles with the aluminium matrix [75]. The ultra-fast cooling process, which is the main feature of metal additive manufacturing, not only suppresses the diffusion reaction kinetics, resulting in the formation of a sharp and clear reinforcement–aluminum interface but also enables the spontaneous engulfment of reinforcing particles (for example, TiB_2 particles in [76]) inside

aluminum grains, as a result of the much higher rate of solidification front as compared to the critical moving velocity of particles. This intragranularly distributed reinforcement allows for more plastic deformation of the Al matrix before fracture by lowering stress concentration at grain boundaries (GBs). It also produces a significant elastic stress/strain field to facilitate the accumulation of dislocations, thereby combining the most two crucial characteristics for enhancing ductility in aluminium matrix composites; that is high fracture tolerance and high strain hardening capacity. (3) Heterogeneous grain structure design in the as-built composites. The non-homogenous cooling rate in melt pool as well as the layer-wise building nature of AM could induce non-homogenous thermal history and the associated microstructures in the as-built parts. These heterogeneous grain distributions introduce the nonuniform distribution of dislocations and the plastic strain gradient, which created high-density GNDs and the resultant hetero-deformation-induced (HDI) hardening, a main mechanism contributes to the enhanced ductility [77]. The combination of one or all of these microstructural designs could endow AM AMCs with improved tensile properties at severe working conditions.

In summary, TiB_2 and TiC have emerged as the most effective reinforcements for AM Al-based composites, primarily by promoting grain refinement and stabilizing the microstructure against coarsening up to ~300–350 °C. However, their efficacy is inherently constrained by the thermal stability limits of the Al matrix and its precipitates. Beyond this temperature, accelerated coarsening of intermetallic phases and a decline in load transfer capability lead to significant softening. This fundamental low-to-medium temperature cap, coupled with the ever-present challenge of balancing strength gains with ductility loss, defines the primary design boundary for AM Al MMCs in extreme environments.

2.2. Titanium Matrix Composites (TMCs)

Titanium-based materials with a unique combination of exceptional corrosion resistance, low density, low thermal expansion, high melting point, good biocompatibility, and high specific strength that is maintained at 400 °C make them competent for various fields such as the automotive, aerospace, military, chemical, and biomedical industries [78,79]. The AM approach, which employs a controlled melt pool dynamic management, could reduce particulate agglomeration and promote an even dispersion of reinforcing particles inside the matrix for enhanced strengthening. The most popular titanium alloy, Ti6Al4V, is noteworthy due to its unique α + β phase microstructure and superior compatibility with reinforcing agents, making it a primary choice for TMCs [80]. Although AM Ti6Al4V possesses excellent qualities, the appearance of oxidation, creep, and phase instability restricts its use at temperatures over 400 °C [81]. To enhance the mechanical strength, several boron, nitride, and carbide-based reinforcements, including TiB, TiC, SiC, and TiN particles, have been applied to AM Ti alloys, yet their strengthening effect shows strong dependence on printing parameters and reinforcing phases. As can be seen from the reported tensile results, boride particles are determined to be the most suitable reinforcement among all of them, presumably due to their comparable density and coefficient of thermal expansion (CTE) to titanium alloys.

To provide strong interfacial bonding in AM TMCs for enhanced tensile properties under different working conditions, effective nucleation sites, dislocation interactions, improved work hardening mechanisms, and thermal compatibility all need to be considered. TiB is found to significantly enhance the strength and ductility of AM titanium composites due to its strong interfacial bonding, excellent thermal stability, and efficiency in pinning grain boundaries for grain refinement [82]. On the other hand, carbide (e.g., TiC) may partially disintegrate under laser irradiation at high temperatures, which could react with Ti and result in the formation of the brittle Ti_2C reaction product. Moreover, TiC can be

oxidized to form surface oxides, where a chemical reaction between the titanium matrix and the oxidation layer occurs, leading to additional interfacial instability and restricting the mechanical property improvement of the AM TMC [21]. These detrimental effects may be mitigated in TiB/TiB_2 composite systems. The 2%TiB/Ti6Al4V composite obtained by L-PBF displayed superior tensile strength at room and elevated temperatures, reaching a promising value of 926 MPa at 500 °C with an elongation of 10.2% [41]. In a titanium-rich condition, TiB_2 transforms into TiB whisker clusters attributed to the dynamically more stable TiB phase. It has found that both the AM Ti6Al4V alloy and the TiB/Ti6Al4V composite had typical columnar prior β-grains with a lot of α/α' laths due to epitaxial growth in the building direction, as shown in Figure 3a,b [83]. Upon solidification, the presence of TiB whiskers encourages the nucleation of finer α and β grains by lowering the critical energy barrier for grain nucleation and coarsening. Therefore, the spacing of α/α' laths and the size of β grains in AM composites are much finer than those of the base L-PBF Ti6Al4V alloy, increasing the yield strength of the AM composite, as shown in Figure 3c,d [84]. Also, no debonding was found at the TiB/Ti interface in the tensile-fractured samples, because of the strong interfacial strength with small lattice misfit.

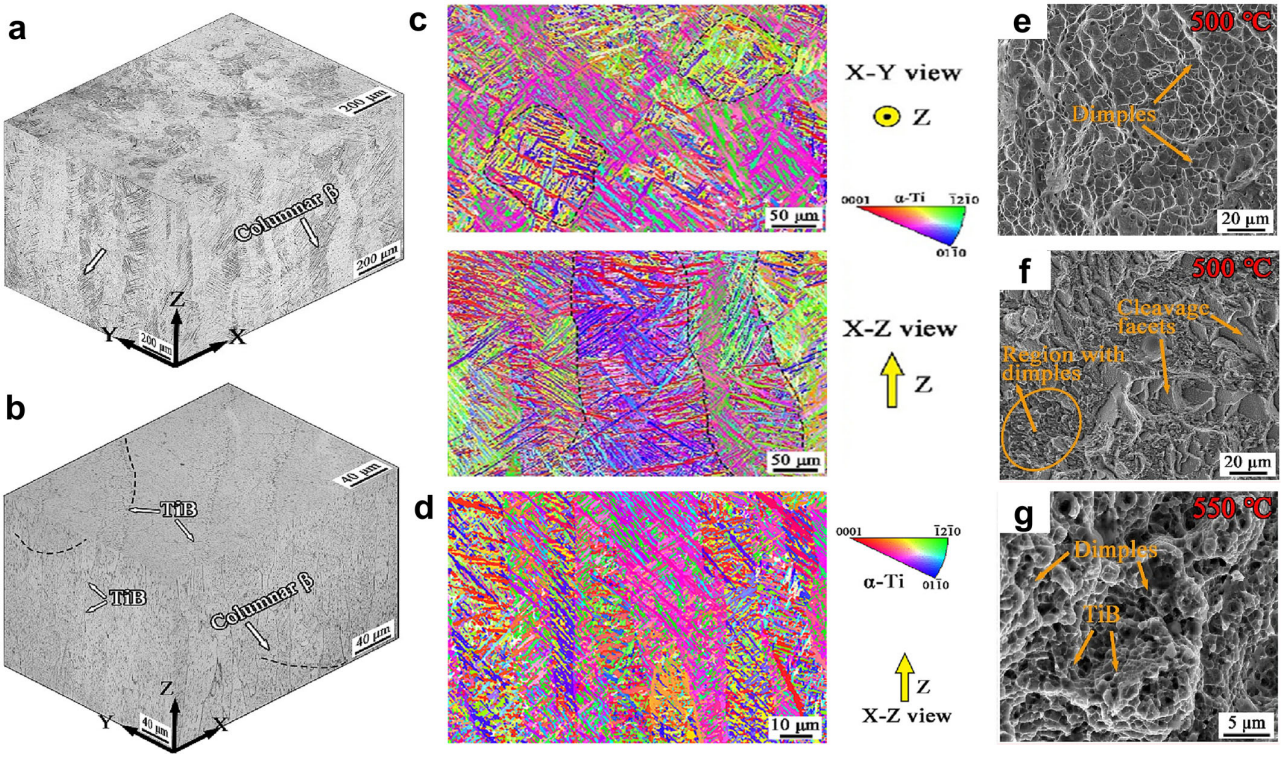


Figure 3. Pseudo-three-dimensional OM image of the (**a**) Ti64 alloy, (**b**) TiB/Ti6Al4V composite, (**c**) inverse pole figures (IPFs) of Ti64 collected from the XY and XZ sections, (**d**) IPF of TMC collected from the XZ section. Fracture morphology of Ti64 alloy after tensile deformation at (**e**) 500 °C. Fracture morphologies of TMC after tensile deformation at (**f**) 500 °C, (**g**) 550 °C. Adapted with permission from Ref. [41]. 2023, Elsevier.

Furthermore, the L-PBF Ti6Al4V composites exhibited higher tensile strengths below 600 °C than the bare L-PBF Ti6Al4V matrix due to the fine microstructure and improved load-bearing capability of TiB, reaching an ultimate tensile strength of 723 MPa at 550 °C, as shown in Figure 1b. It has been observed that the L-PBF TiB/Ti6Al4V strengthening effect progressively diminished as the temperature increased to 600 °C, where the degradation of fine-grain strengthening and the interface debonding between the matrix and TiB whiskers are responsible for the lack of additional strengthening. For the bare AM Ti6Al4V alloy, as

the temperature increased, a typical ductile fracture with several dimples was observed with a deepened and stretched morphology, as shown in Figure 3e. More specifically, a mixed fracture mode, with cleavage facets and dimple regions, was observed in Ti-6Al-4V at 500 °C, indicating a combination of brittle and ductile fracture mechanisms, as shown in Figure 3f. When the temperature increases to 550 °C, the fracture morphology of the AM composite comprises dimples without cleavage facets, agreeing with the noticeably increased ductility, as shown in Figure 3g. The dimples were relatively tiny and did not extend on a larger scale, in contrast to the distorted microstructure of the base AM Ti64 alloy, suggesting the higher tensile ductility. However, due to the breakdown of grain-refinement strengthening and the interfacial decohesion between the TiB whisker and the Ti64 matrix as the temperature increased to more than 600 °C, the strength enhancement of AM composites was severely restricted, and ductility was remarkably reduced [41].

Notably, there are some unique strengthening effects in AM Ti-based composites ascribed to the non-equilibrium solidification feature. The interactions between various phases within the composite, the solidification process, and the complex melt pool dynamics are the main variables influencing the microstructural evolution. Extremely high cooling rate and repeated thermal cycles are the main features of AM processing. Upon solidification, the material does not have enough time to reach an equilibrium state as a result of the fast cooling. This could lead to phase stabilization and distinct microstructures as compared to conventional methods [85]. Zhang et al. [86] found that the microstructure and phase transformation of Ti-5553 alloy are significantly influenced by the addition of 5% Mo during L-PBF. This addition leads to substantial columnar-to-equiaxed transition (CET) and grain refinement, as shown in Figure 4a,b. This is primarily because Mo acts as a strong β-stabilizer, which significantly suppresses the martensitic shear transformation of the β phase to α' during the rapid cooling of L-PBF. The enhanced β stability promotes a diffusion-controlled $\beta \rightarrow \alpha$ transformation pathway, facilitating the formation of equiaxed α grains during subsequent solid-state phase transformations. Specifically, Mo contributes to grain refinement in two main ways. (1) Mo nanoparticles that survive partial melting act as heterogeneous nucleation sites for the new grains. (2) The dissolution of Mo particles surrounding the solid core potentially generates a supercooled region that enhances the heterogeneous nucleation efficiency of partially melted Mo particles. This stabilization effect arises because Mo, as a strong β-stabilizer, lowers the martensitic start temperature and suppresses the formation of α and ω phases during rapid cooling. The resulting homogeneous β phase distribution enhances microstructural uniformity and contributes to improved mechanical consistency, as shown in Figure 4c–e [87]. Thus, the 5% Mo + Ti-5553 sample exhibited improved ductility, more consistent tensile properties, and superior strength. The strength enhancement is attributed to both grain refinement and solid solution strengthening from the Mo solute, while improvement in ductility is mainly ascribed to the Mo solute's suppression of metastable phase precipitation, rather than effects like the transformation-induced plasticity. In addition, it was reported that the L-PBF B_4C-reinforced Ti6Al4V composite has better properties at 500 °C as compared to that deformed at room temperature, as shown in Figure 1a,b [88]. This improvement can be attributed to two synergistic effects enabled by the L-PBF process: firstly, the in situ-formed TiB needles effectively pin grain boundaries, enhancing microstructural stability at elevated temperatures; secondly, the ultra-fast solidification of L-PBF results in a supersaturation of carbon atoms in the α-Ti matrix, which provides persistent solid solution strengthening up to 500 °C before significant diffusion and precipitation occur. The main reason for this abnormal "higher strength in higher temperature" behavior was due to the fact that carbon is dissolved and in a solid-solution state in the solidified α-Ti phase because the α-Ti structure, with its hexagonal close-packed (hcp) arrangement, can accommodate small

amounts of carbon atoms in interstitial sites [89,90]. At elevated temperatures, the solubility of carbon in α-Ti increases, allowing more carbon to dissolve into the lattice. This dissolution strengthens the material through solid-solution strengthening, as the carbon atoms distort the titanium lattice, impeding dislocation movement. Moreover, carbon stabilizes the α-phase, preventing its transformation to the softer β-phase at higher temperatures [91]. This combination of solid-solution strengthening and phase stabilization is responsible for the higher strength of the material at elevated temperatures.

To conclude, the high-temperature performance of AM Ti-based composites is governed by a synergy between in situ-formed reinforcements (e.g., TiB whiskers) and solid-solution strengthening, enabling useful strength retention up to 500–550 °C. The non-equilibrium AM process is crucial in facilitating unique mechanisms such as carbon supersaturation in α-Ti. Nevertheless, the overriding challenge remains the oxidative instability and phase transformations in the Ti matrix above 400 °C, which often poses a more severe limitation than the strength of the reinforcement itself. Furthermore, managing the anisotropy from prior-β grains and the complex stress states around in situ-formed phases is critical for achieving reliable performance.

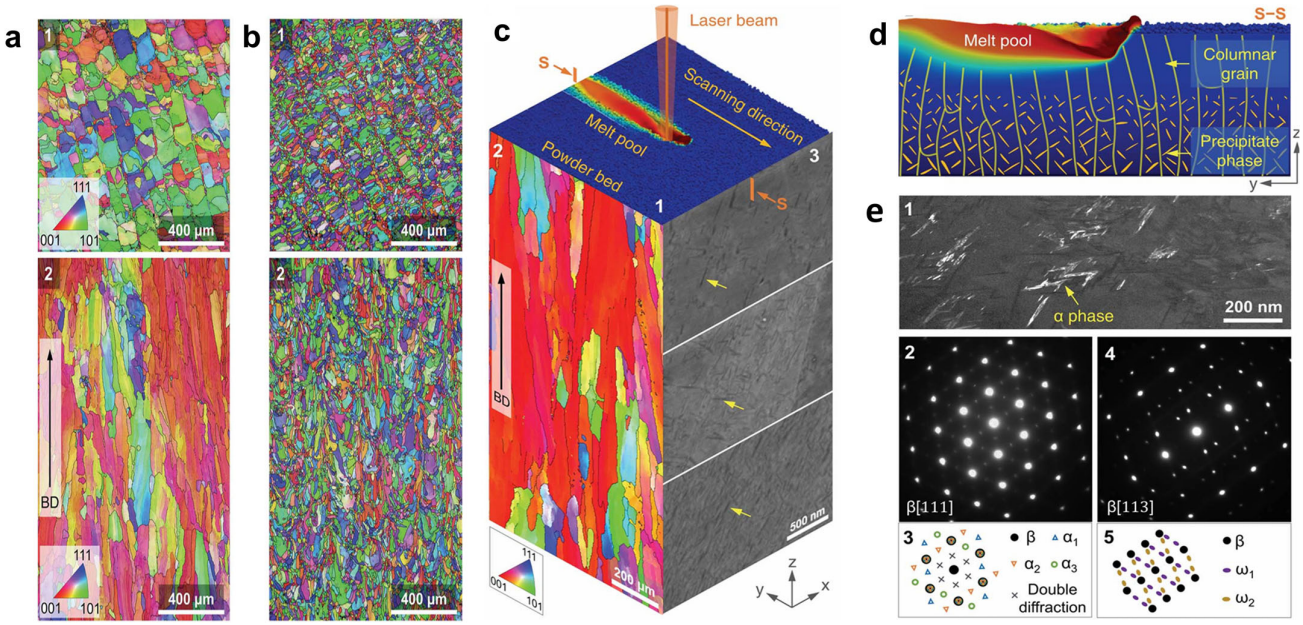


Figure 4. (**a**) Electron Backscatter Diffraction (EBSD) IPF maps (1) and the xz-plane (along the building direction) (2) of the Ti-5553 sample. (**b**) EBSD IPF maps of the xy-plane (1) and xz-plane (2) of the Ti-5553 + 5Mo sample. (**c**) The coexistence of coarse columnar ß grains and spatially dependent phases in Ti-5553 produced by L-PBF. (**d**) Schematic illustration of the microstructure heterogeneity in terms of columnar ß grains and heterogeneously distributed phases on the cross-section S−S (the yz-plane), as indicated in (**c**). (**e**) Transmission electron microscope (TEM) micrographs of Ti-5553, (1) dark-field TEM image showing α phases, (2) TEM selected area electron diffraction (SAED) pattern from the $[111]_{ß}$ zone axis showing the presence of α phases. The key diagram of the diffraction is shown in (3). Note that there are three variants with the same zone axis of 2110, which grow in different directions. (4) TEM SAED from the $[113]_{ß}$ zone axis showing the existence of isothermal ω phases. The key diagram of the diffraction is shown in (5). Note that there are two ω variants. Adapted with permission from Ref. [86]. 2024, The American Association for the Advancement of Science.

2.3. Nickel Matrix Composites

Conventional nickel-based alloys, due to their great strength and resistance to corrosion at temperatures between 650 °C and 1000 °C, are used in the production of critical

hot-end components in industrial gas turbine engines, seawater pipelines, aerospace, and other fields [92–94]. Remarkably, the aircraft manufacturing sector will need more and more intricate structural designs and high-temperature components in the future. These exceptional qualities, however, make it challenging to process these materials using traditional production techniques due to concerns like high cost and energy consumption. Therefore, using a high-energy-density laser beam as a heat source and a high degree of machining freedom, AM has been gradually taken into account to obtain Ni-based hot-end components with complex structures and exceptional performance.

We summarized the state-of-the-art study on tensile properties of AM nickel-based composites targeted for extremely demanding in-service applications. Several carbide, boride, and oxide-based ceramics, including TiC, TiB_2, ZrB_2, SiC, Y_2O_3, and Al_2O_3, have been widely employed in nickel alloys to enhance the high-temperature performance [11]. However, similar to AM aluminum composites, many reinforcements are not suitable for AM processing because of their self-decomposition at high temperatures or extensive chemical reactions with the Ni matrix. For instance, for composites reinforced with Al_2O_3 particles, Al_2O_3 thermally decomposes and releases oxygen into the melt pool during AM, which introduces porosity and high aluminum content surrounding these pores [95]. Moreover, the AM process intrinsically encompasses multiple heating–cooling cycles, upon which these oxides can cause thermal mismatches with the nickel matrix to induce localized stress under high-temperature gradients, giving rise to local stress concentration at interfaces to form microcracks. For another typical SiC reinforcement, the reinforcing particles are observed to show either partial or total dissolution during the melting phases, followed by reprecipitation when the temperature is not high enough to cause decomposition, enabling a much finer particle size than the original ones. However, the distribution of SiC particles in the as-built samples is not uniform, forming a band-like morphology that acts as heterogeneous nucleation sites, leading to localized columnar grain growth [96].

TiB_2 and TiC particles are generally demonstrated to have the potential to facilitate the creation of complicated, crack-free AM Ni-based composites, as demonstrated by the property summary figure in Figure 1. This could be attributed to the following reasons. Firstly, the relatively high thermal conductivity of these particles contributes to more uniform temperature gradients by facilitating better heat dissipation during the melting and cooling cycles, which reduces the thermal stresses and avoids distortions or cracks in parts. Secondly, these particles are thermally stable and have a high melting point, which can serve as a highly efficient nucleation agent during solidification, promoting homogeneous grain growth and creating uniform microstructure [97]. This uniform, refined microstructure improves the material's capacity to accommodate thermal contractions on a larger scale, lowering residual stresses. Thirdly, the nucleation efficiency of particles is further amplified by the low lattice mismatch between reinforcing particles and the nickel matrix. It is known that nickel has a face-centered-cubic (FCC) crystalline structure with a lattice parameter of ~3.52 Å, while the representative TiB_2 has lattice parameters of 3.22 Å. The discrepancy in these characteristics indicates a lattice mismatch that could influence the bonding quality between these particles and nickel alloys, because grain nucleation, interfacial bonding, and the microstructure are all (or at least partially) determined by the lattice mismatch. Higher nucleation rates and reduced interfacial energy are the results of a smaller lattice mismatch [98].

The AM Ni-based composites could significantly improve the tensile properties of Ni alloys at elevated temperatures. Notably, the 2% TiB_2/IN718 composite displayed 17.62% improvement of tensile strength at a testing temperature of 650 °C as compared to AM IN718 alloy, reaching 963.6 MPa (the highest value among all the AM Ni-based composites, as shown in Figure 1a,b. The incorporation of TiB_2 nanoparticles was found to decrease

the size of the equiaxed Ni grains, with the average grain size of L-PBF IN718 alloy and 2% TiB_2/IN718 to be 13.21 μm and 8.83 μm, respectively, as shown in Figure 5a,b [39]. More specifically, three main reasons are reported to be responsible for this improved strengthening effect at high temperatures. (1) The addition of TiB_2 particles increased the number of nucleation sites and promoted heterogeneous nucleation [99]. (2) These reinforced particles pin the grain boundaries of the solidified part, which prevents the grains from coarsening in the subsequent heating/cooling cycles. Grain refinement can lead to a significant strengthening based on the Hall–Petch relation, and more importantly, hinders the grain-boundary-dominated softening behaviors at high deformation temperature. (3) TiB_2 and IN718 matrix possess remarkably different CTE, which is 6.4 [100] and 13.16 × 10^{-6} K^{-1} [101], respectively. Therefore, a high density of geometrically necessary dislocations (GNDs) is generated around the interface for enhanced back stress hardening. Importantly, the reinforcing particles are shown to have a positive effect on the decrease in porosity. In composite powders, the reinforcement reduces laser reflection of the Ni alloy powders, eliminating spattering and raising the viscosity of the melt pool. These effects increase energy absorption for more uniform melting and induce fewer unmelted particles that would have hindered the process of solidification [102]. Porosity reduction via composite strategy is another important contribution to the enhanced tensile properties of AM Ni-based composites.

Apart from the incorporation of stable reinforcements for remarkable strengthening, the dissolving, diffusion, and subsequent reprecipitation of reinforcing phases are another way of achieving excellent tensile properties in AM Ni-based composites. ZrB_2 reinforcement is such a kind of example. During L-PBF processing, ZrB_2 first decomposes into Zr and B elements that dissociate in Ni melt, after which the complex elements (Ni, Zr, B, Nb, Mo, and Cr) undergo chemical reactions to produce intricate borides and intermetallic compounds. For instance, the free Zr can react with nearby Ni elements during L-PBF to produce (Zr, Ni)-based intermetallic, and the free B may have diffused into boride-forming elements (Nb, Mo, and Cr) to form complex borides. Therefore, the as-built ZrB_2/In718 composites contain multiple nanophases, including (Nb, Mo, Cr)-rich boride nanoparticles (sizes between 100 and 200 nm) and (Zr, Ni)-based intermetallic nanoparticles (sizes below 200 nm), as shown in Figure 5c. These intermetallics based on Zr and Ni elements are known for their mechanical and thermal stability, enabling them to be an excellent dispersion-strengthening component in the AM Ni-based composites at high deformation temperature. The interactions between compound phases and dislocations have been demonstrated in samples tensile tested at 800 °C, where entangled dislocations and encircling dislocation loops near the dispersed intermetallic nanophases were clearly revealed in the deformation microstructures, as shown in Figure 5d [34].

Grain boundary kinetics is important for the overall mechanical properties of materials deformed at high temperatures. In particular, diffusional mechanisms at the grain boundaries become more noticeable at high temperatures, which could lead to materials with large strain-rate sensitivity ($m = d\ln\sigma/d\ln\varepsilon$, where σ and ε are true stress and true strain, respectively). The damage evolution can, therefore, be changed, and the onset of flow localization (or necking) is delayed based on the Conside're criterion [103]. Except for the interactions between dislocations and intermetallic phases in AM Ni-based composites as mentioned above, the formation of special boron-induced serrated grain boundaries is reported to maintain exceptional ductility, as shown in Figure 5e,f. This boron-induced serrated grain boundaries may possess a higher m value, facilitating a stabilized necking behavior and damage evolution as compared to the AM In718 matrix. Consequently, the AM ZrB_2/In718 composite exhibits 10% higher yield strength and approximately 10 times higher tensile ductility than that of pure In718, at a deformation temperature of 800 °C.

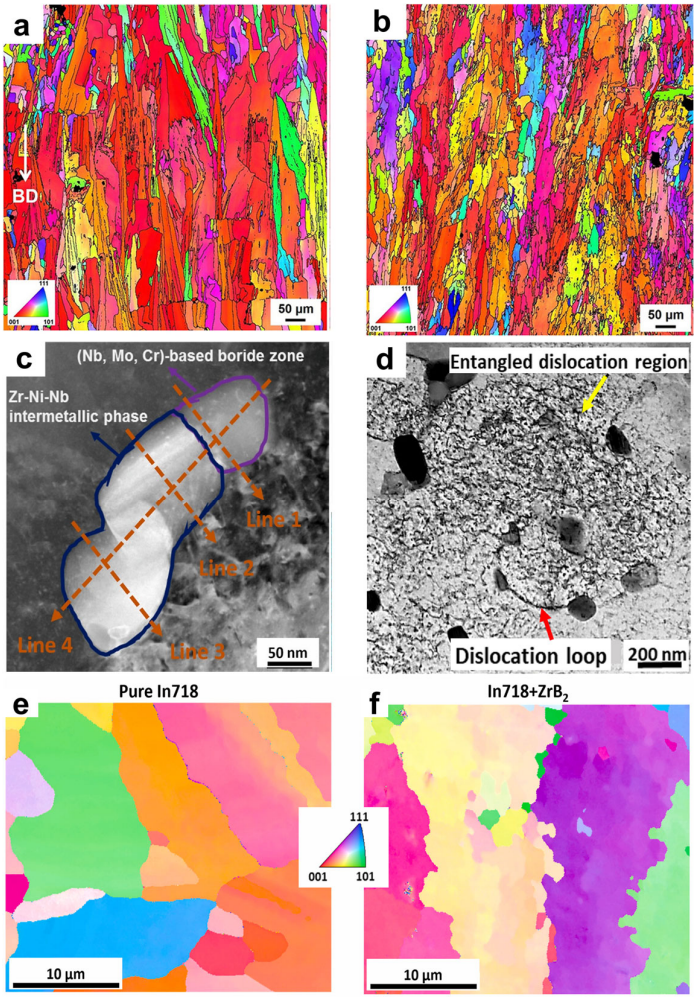


Figure 5. EBSD images (**a**) IN718, (**b**) TiB_2/IN718. Adapted with permission from Ref. [39]. 2022, Elsevier. (**c**) High-magnification scanning transmission electron microscopy (STEM)/energy-dispersive X-ray spectroscopy (EDX) mapping analysis obtained from heat-treated (HT'ed) In718 + ZrB2, focusing on an exchange reaction zone between Zr, B and Nb, Mo, Cr. (**d**) STEM image and EDX mapping obtained from HT'ed In718 + ZrB2 after 800 °C tensile test showing dislocation loop and entanglement in the microstructure. EBSD maps obtained from (**e**) HT'ed In718, (**f**) In718 + ZrB2 showing the difference in grain boundary morphologies. Adapted with permission from Ref. [34]. 2024, Elsevier.

A similar strengthening effect had been reported in some AM nickel composites reinforced by TiB_2 particles. The AM TiB_2/In625 composite exhibits notable improvements in yield strength, ultimate tensile strength, and ductility of 56%, 68%, and 164%, respectively, as compared to bare AM In625 alloy at 800 °C, as shown in Figure 1a,b [33]. Upon L-PBF, TiB_2 acts as a potential source of boron in In625 matrix, where several transition metals, including Cr, Mo, and Nb, interact with boron to create complex boride precipitates. This produces nano-dispersed (Ti, Al, Nb)-oxide phases within the matrix and (Cr, Mo)-boride phases near the grain boundaries, which improve the high-temperature properties and prevent the formation of detrimental high-temperature phases, as shown in Figure 6a. The serrated GB motion dynamics in AM TiB_2/In625 composite are one of the key mechanisms for the enhanced ductility, similar to AM ZrB_2/In718. It is observed that the serrated grain boundaries could also significantly affect the fracture process of AM nickel-based composites by preventing cracks from spreading along them, as shown in Figure 6b [104]. The creation of a continuous crack channel is thought to be impeded by the voids and cavities along these serrated grain boundaries, which are thought to hinder facile per-

colation. This impact is most noticeable in working conditions with high temperatures and low strain rates, where diffusional phenomena at grain boundaries control the failure mechanisms [105]. Generally, the development of such serrated grain boundaries has been attributed to the discontinuous segregation of Cr, C, and B elements along the grain boundaries [106], as induced by the preferential diffusion and segregation of alloying elements and variations in lattice strain energy at the boundaries.

For more extreme working conditions, with temperatures ranging from 800 °C to 900 °C, grain refinement may not be the dominant factor, as grain coarsening could occur at these high temperatures. It had been reported that AM TiC-reinforced GTD222 nickel alloy composites still depicted superior tensile properties with yield strength noticeably higher than that of the AM GTD222 matrix. Fine-grain strengthening may not be the main reason for additional strengthening any longer because the average grain sizes in AM composite and bare matrix are comparable (which are 39.7 and 38.6 μm, respectively), Figure 6c–f.

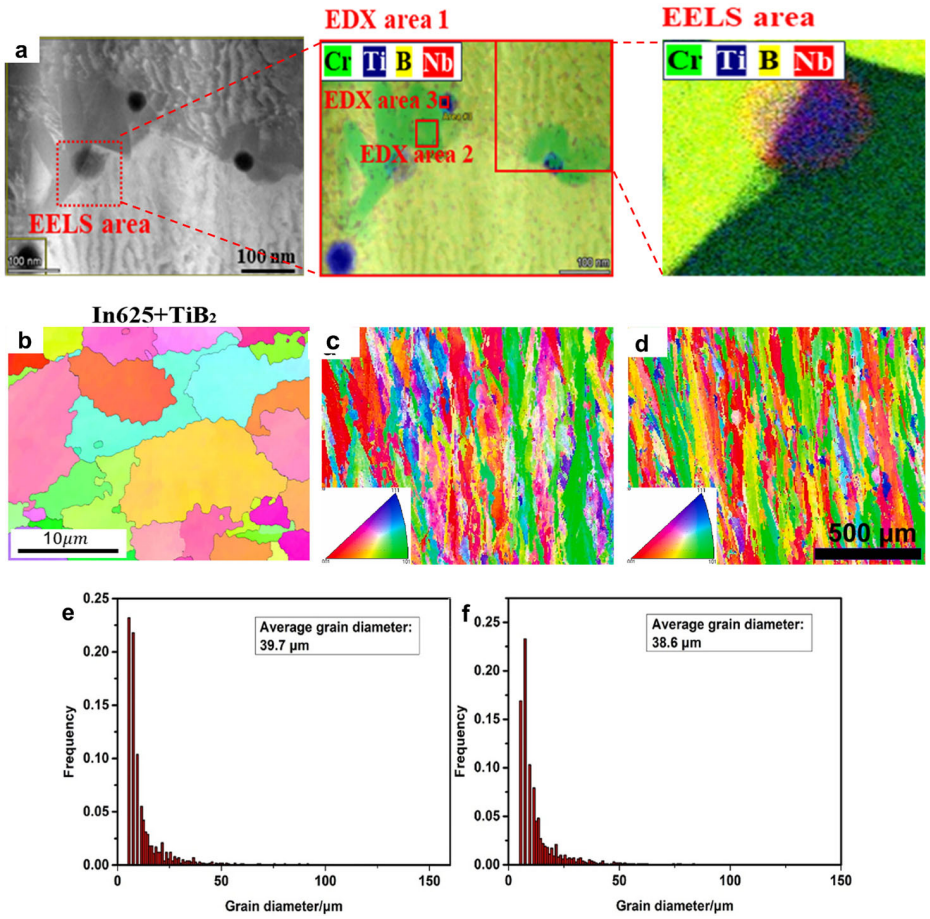


Figure 6. (**a**) Electron energy loss spectroscopy (EELS) and EDX map, revealing B partition in Cr-rich region, (**b**) In625 + TiB_2, as confirmed through IPF maps. Adapted with permission from Ref. [33]. 2024, Elsevier. The EBSD IPF maps of heat-treated (**c**) GTD222 and (**d**) TiC/GTD222 corresponding to grain size distributions. (**e**) Grain size distributions of GTD222, (**f**) grain size distributions of TiC/GTD222 composite. Adapted with permission from Ref. [38]. 2022, Elsevier.

It is found that the plastic deformation mechanisms of the composite at elevated temperatures are complex, which include dislocation slip within the γ matrix, dislocation pairs shearing γ′ produce anti-phase boundary, isolated stacking faults shearing γ′ phases, and continuous stacking faults shearing γ and γ′ phases, as shown in Figure 7a,b. In AM TiC/GTD222 composite, stacking faults within γ′ can hinder the shearing action of the mobile dislocation during the plastic deformation at 800 °C, giving rise to the additional

strengthening, as shown in Figure 7c,d [38]. Moreover, the dislocation density of the AM TiC/GTD222 composite is somewhat greater than that of the AM GTD222 alloy because of the thermal misfit at interfaces and the resultant local dislocation accumulations, as shown in Figure 7e. Thus, the increase in yield strength in the composite is mainly due to the enhanced dislocation blockage on slip planes and is assisted by the additional dislocation strengthening. At a more extreme high temperature of 900 °C, 1% TiB_2 was reported to render more strength improvement for the AM GH3230 nickel alloy [36]. The TiB_2 particles dispersed throughout the matrix to make a pinning effect during elevated temperatures, as shown in Figure 7f, which controls the sliding of grain boundaries and reduces the dislocation climbing rate, thereby enhancing the tensile strength of the AM Ni-based composites [37].

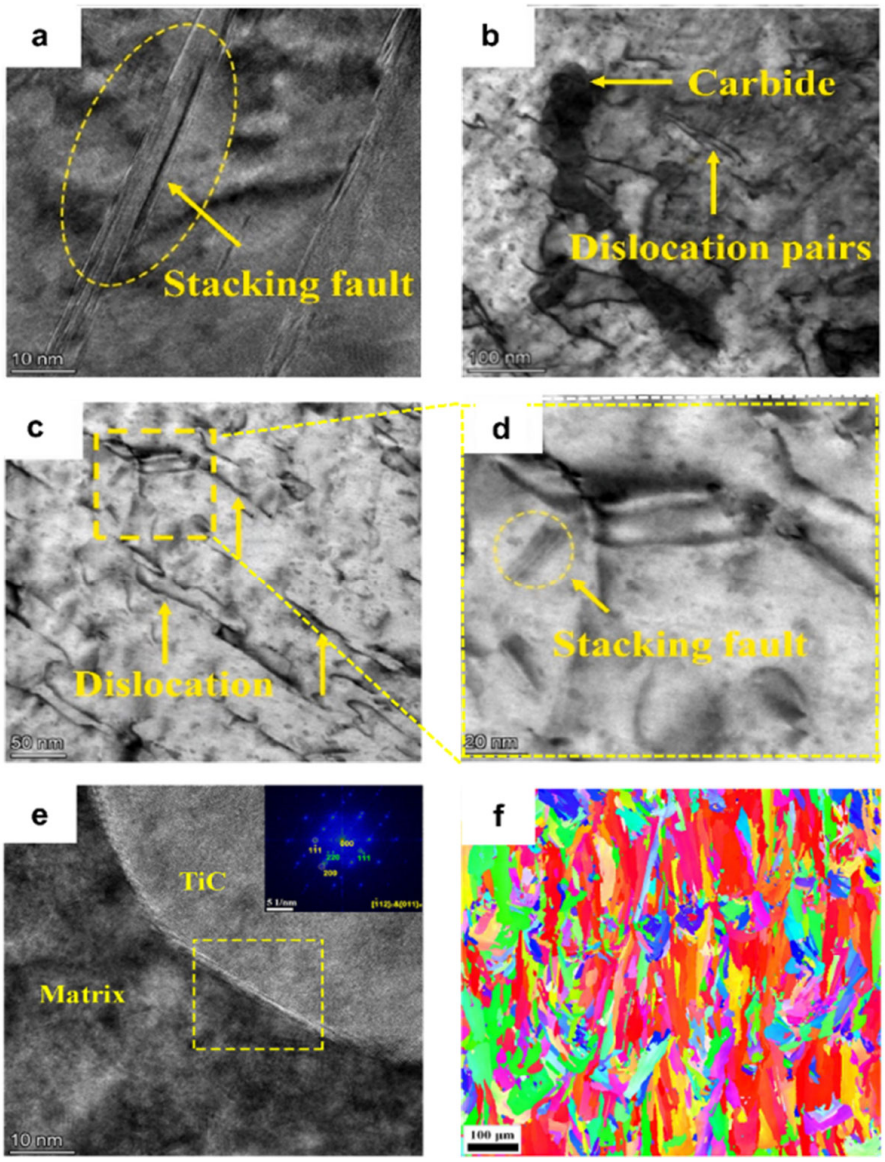


Figure 7. (**a**) Continuous stacking faults, (**b**) dislocation pairs, (**c**) dislocations, (**d**) stacking fault. TEM images of TiC and matrix in TiC/GTD222 composite: (**e**) the interface image of TiC and matrix. Adapted with permission from Ref. [38]. 2022, Elsevier. (**f**) EBSD image of 1%TiB_2/G3230. Adapted with permission from Ref. [37]. 2022, Elsevier.

In summary, AM Ni-based composites achieve exceptional high-temperature tensile performance (650–900 °C) through a combination of grain refinement, innovative

microstructural features like serrated grain boundaries, and, most notably, in situ precipitation hardening from decomposed reinforcements (e.g., ZrB_2). This ability to create stable nano-dispersoids within the matrix represents a key advantage over ex situ particle addition. The primary trade-off, however, lies in the extremely narrow processing window required to avoid defects (cracks, porosity) induced by reinforcement–matrix interactions or thermal stresses, making process optimization paramount for success in this system.

2.4. Steel Matrix Composites

The extremely nonequilibrium microstructures produced in FCC austenite steels (such as 316L and 304 stainless steels), represented by the ultrafine dislocation cells and local solute segregations, are attributed to the non-homogeneous thermal gradient and rapid solidification process upon AM [107]. L-PBF steels and other AM steels are typically far stronger than their conventional counterparts, which is mainly attributed to the ultrafine dislocation cells that are intrinsically present in the as-built samples [108]. These AM steels contain low-angle grain boundaries that are usually coincident with the dislocation cell boundaries, with solute segregation along the cellular walls. The ultrafine, dense dislocation cells could serve as sources of gliding dislocations as well as a weak barrier for their propagation, producing moderate but sustained dislocation accumulation capacity [109]. The elemental segregation at dislocation cell walls further improves dislocation pinning as well as promotes twinning, boosting the material's strength and ductility of AM austenite steels [110].

Dislocations in AM steels mostly undergo dislocation slip at high temperatures. However, as compared to tensile deformation at room temperature, where dislocations consistently interact and organize into smaller dislocation cell structures as the material deforms, the recovery process takes control at high temperatures. It was proposed that dislocations can be annihilated and rearranged at a much higher rate due to thermal activation and the presence of dense pre-existing dislocations, which decreases the dislocation density inside the cells and reduces the work hardening capacity [111]. Interestingly, dislocation cell structures in AM FCC steels are found to be much more thermally stable than conventional dislocation cells in austenite steels. Li et al. [112] reported that the stabilization of dislocation cell structures in AM 316L stainless steel is the result of chemical micro-segregation at cell boundaries, mainly Cr and Mo, as shown in Figure 8a. Above 600 °C, the elements' micro-segregation begins to diffuse, and the dislocation cell structure loses its strengthening effect, as shown in Figure 8b. The dislocation structure and elemental micro-segregation are completely eliminated above 1000 °C, as shown in Figure 8c. To further understand the stability mechanism, the thermal stability of the unique dislocation cellular substructures in AM stainless steels (SS), such as 316L SS, 304L SS, and Al-modified 316L SS, and their effects on recrystallization at high temperatures were systematically investigated by Deng et al. [109]. It was demonstrated that the stability of dislocation cells in AM materials, which further impacts the material's ability for recrystallization, depends critically on the segregation of heavy elements (such as Mo) and stacking fault energy (SFE), controlled by Al addition, as shown in Figure 8d,e. More specifically, the incorporation of Al can lead to high SFE, which can dramatically lower the thermal stability of the dislocation cellular structures in AM austenitic SS and also decrease the dislocation density on cellular walls in the as-built material, as shown in Figure 8f,g. Because of its rapid recovery at high temperatures, recrystallization is not possible in high SFE AM 316L(Al) SS. It was found that the significant cellular wall breakdown began at 700 °C in AM 316L SS, 600 °C in AM 304L SS, and 500 °C in AM316L(Al) SS [109]. The pinning effect by atom segregation at dislocation cell boundaries can limit dislocation movement and further stabilize the cell structure under high stress, preventing the growth of cell structures. Stabilization may also

be facilitated by interactions between various dislocation types, as different dislocation types may arise within cellular structures because of the chemical heterogeneity-induced variations in local SFE. The dislocation-type diversity is beneficial to maintain an equilibrium state between recovery and hardening mechanisms, which eventually stabilizes the cell structure.

Overall, the strength of AM austenitic steel composites stems from their unique dislocation cell structure, which can be further refined and stabilized by nano-reinforcements (e.g., TiC, CNTs). This provides outstanding room-temperature properties and stability up to ~600 °C. However, the very foundation of this strength—the metastable dislocation cells and associated solute segregation—becomes its Achilles' heel at higher temperatures. The breakdown of this cellular structure due to recovery and diffusion above 600–700 °C leads to a rapid decline in strength, highlighting a fundamental temperature limit for this strengthening mechanism and directing future efforts towards stabilizing these substructures at even higher temperatures.

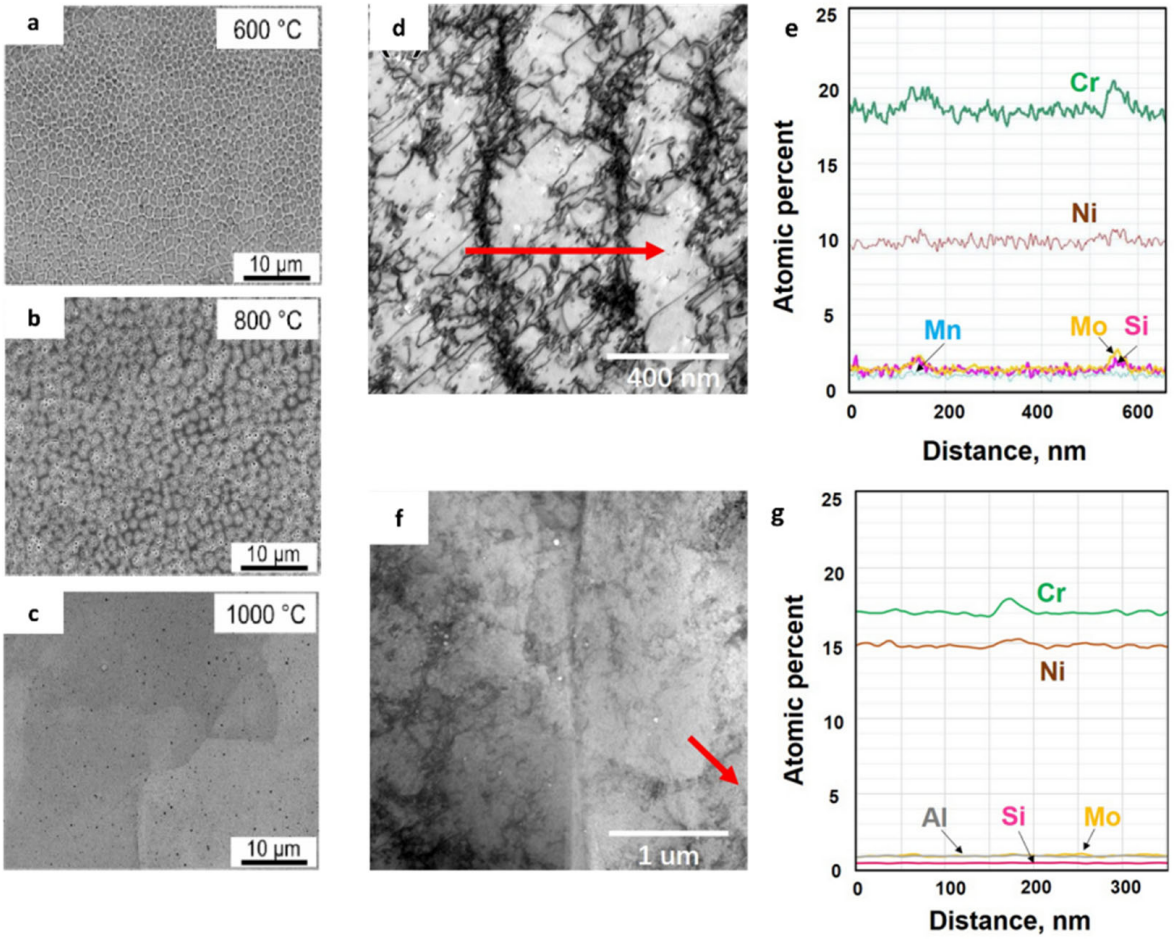


Figure 8. SEM micrographs of AM 316L stainless steel (**a**) 600 °C, (**b**) 800 °C, (**c**) 1000 °C. Adapted with permission from Ref. [112]. 2023, Elsevier. TEM image and EDS line scan of the cellular boundary showing the elemental segregation at the cellular wall of (**d**,**e**) AM 316L(Al) SS and (**f**,**g**) AM 316L(Al) SS. Red arrows represent the EDS line scan location. Adapted with permission from Ref. [109]. 2020, Springer Nature.

Despite the thermal stability, the strengthening contribution from dislocation cells decreases as the temperature rises, as dislocation recovery intensifies at elevated temperatures. More broadly, the reduced tensile strength of AM fcc steels can be ascribed to the following aspects: (1) Stacking fault energy in AM steels increases with temperature. Higher SFE

enables easier dislocation climbs and cross-slips, making it easier for them to go around obstacles (i.e., reduced dislocation blockage). Molnar et al. reported that [113] in 316L steel, as the temperature rises, the stacking fault energy increases, leading to progressively smaller separations between partial dislocations and the tendency for twinning decreases. Thus, increased SFE efficiently suppresses twinning, particularly at higher temperatures, by raising the critical stress required for twinning because the energy barrier for glide is substantially lower than that of twinning or other mechanisms, and dislocation glide takes over as the main deformation mechanism at 500 °C [114]. (2) High temperatures reduce the effectiveness of alloying element segregation at dislocation boundaries. Dislocations can move more freely as the pinning effect decreases, as these segregated atoms diffuse or dissolve into the matrix. (3) Nanotwins are dynamically created during deformation processes and act as strong obstacles to dislocation motion, which improves both the strength and ductility of the AM steels deformed at room temperatures [115]. However, nano twins are dissolved at high temperatures, which loses their strengthening effect.

Here, we mainly pay attention to the deformation mechanisms of AM austenite steel matrix composites at high/low temperatures, and the principles of the composite strategy for property enhancement are believed to be applicable to other kinds of AM steels. Notably, in a TiB_2-reinforced steel alloy, both the 316L and TiB_2 phases are evident in the microstructures and distributions of the Fe, Ti, and B elements, demonstrating that SLM was effective in manufacturing TiB_2/316L nanocomposites [116]. The TiB_2 nanoparticles impede the growth of the grains by acting as heterogeneous nucleation sites. However, there is some degree of segregation of the alloying elements inside the solidified nanocomposites, especially for the greater amount of TiB_2, indicating that micro-segregation occurs at the cellular structure boundaries. For the AM 10%TiB_2/316L composite, Ti-based particles are mostly homogeneous and are distributed at both the boundaries and inside of the dislocation cells, as shown in Figure 9a–c. This modification of the dislocation cell structure efficiently suppresses the DRV and DRX at high deformation temperatures, demonstrated by the lack of microstructure changes at 700 °C. As a result, the AM 10% TiB_2/316L has higher strength than 5% TiB_2/316L at 700 °C across the entire strain range and also exhibits a noticeably greater strength at low strain at 800 °C, as shown in Figure 9d,e. While microstructural evolution usually occurs during elevated temperature deformation, this AM 10% TiB_2/316L composite exhibits no observable changes in either the cellular or grain structures. The post-mortem microstructure analyses indicate that micro-segregation persisted at the cellular structure boundaries of the composite after deformation, as shown in Figure 9f,g. These Ti-based dispersoids and enhanced pinning by micro-segregation via TiB_2 particle incorporation are considered to facilitate the thermal/mechanical stability of the cellular structures [117]. This greatly suppresses microstructure evolution, and correspondingly, improves the mechanical properties at high deformation temperatures of AM austenitic stainless steels.

The AM austenitic steels are also promising materials for low-temperature applications requiring high strength and phase stability. In particular, 316L stainless steel produced by AM is attractive due to its high strength, outstanding corrosion resistance, and exceptionally low ductile-to-brittle transition temperature. Wang et al. [118] found that the distinct cellular structure and grain texture of L-PBF 316L stainless steel significantly influence its cryogenic mechanical properties. The as-built sample exhibits a well-defined intragranular cellular structure (~0.5 μm in size) and columnar grains with a weak <110> texture along the building direction, as shown in Figure 9h,i. It demonstrates high strength at −196 °C, with a yield strength of 840 MPa, an ultimate tensile strength of 1510 MPa, and a promising elongation of 35%. The primary reason for its extremely high strength and strain hardening is the strain-induced martensitic transformation, which dynamically strengthens

the material and leads to multistage strain hardening behavior. The stacking fault energy of 316L SS decreases with lowering temperature, facilitating the formation of α′-martensite during plastic deformation. This martensitic transformation is further accelerated by the ultrafine cellular structure, which promotes the nucleation of shear bands and increases nucleation sites for α′-martensite. Therefore, the stability of the cellular structure at low deformation temperatures is crucial for the remarkable strengthening effect. Tuning cellular structure stability through chemical modifications or physical pinning in AM steel-based composites can enhance strengthening mechanisms at cryogenic temperatures. Although rarely studied so far, the mechanical properties of AM steel-based composites at low temperatures are scientifically intriguing and could greatly expand the applications of AM steels.

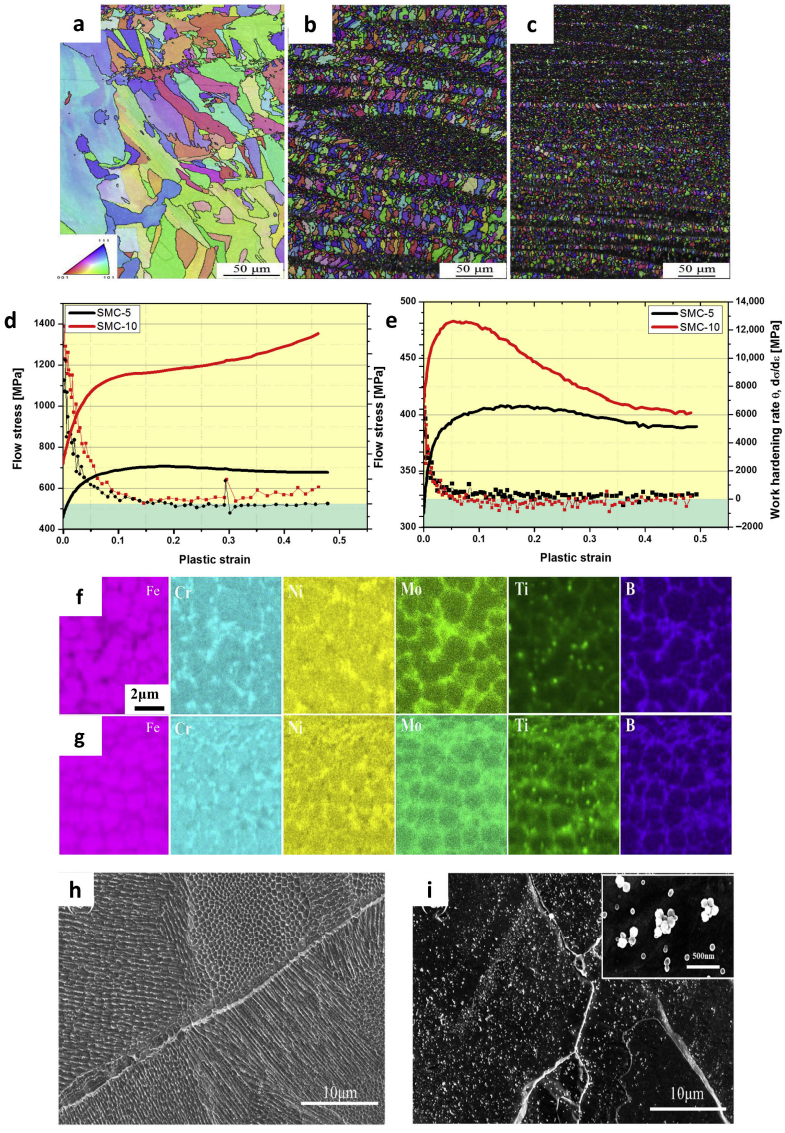


Figure 9. Low-magnification grain orientation maps of (**a**) 316L alloy, (**b**) 5% TiB_2, and (**c**) 10% TiB_2. The grains are significantly refined after adding TiB_2 particles. Flow curves at (**d**) 700 °C and (**e**) 800 °C experimentally measured work hardening rate θ ($d\sigma/d\varepsilon$) obtained from the flow curves for5% TiB_2 and10% TiB_2. EDS mapping of (**f**) 5% TiB_2 and (**g**) 10% TiB_2. The micro-segregation phenomenon occurs at the boundaries of cellular structures in the nanocomposites. Adapted with permission from Ref. [116]. 2019, Elsevier. (**h**,**i**) Intragranular substructure of as-built and HT. Adapted with permission from Ref. [118]. 2021, Elsevier.

2.5. Critical Synthesis and Comparative Analysis of Tensile Performance

The preceding sections have detailed the room- and elevated-temperature tensile behaviors of AM MMCs across four major alloy systems (Al, Ti, Ni, and steel). To advance the field beyond phenomenological reporting, a critical synthesis must move from isolated observations to a comparative perspective that identifies overarching principles, matrix-dependent trends, and common trade-offs. The following analysis first consolidates key data to enable cross-system comparison, then elucidates the underlying mechanisms and challenges that define the performance landscape of AM MMCs.

The comparative data in Table 1 underscores a fundamental principle: the effectiveness of a ceramic reinforcement is profoundly matrix-dependent, governed by interfacial stability and thermodynamic compatibility. In Al-based systems, TiB_2 and TiC excel due to limited interfacial reaction and potent grain refinement, whereas conventional SiC often degrades. Conversely, in Ni-based superalloys, both TiB_2 and TiC perform well, but their strengthening manifests differently—TiB_2 primarily through grain refinement and load transfer, while decomposing reinforcements like ZrB_2 introduce potent nano-scale precipitate hardening. For Ti alloys, TiB is superior to TiC due to its excellent compatibility and in situ whisker formation. This matrix–reinforcement symbiosis negates the concept of a universal "best" reinforcement; selection must be dictated by the specific metallic matrix and the target temperature regime.

Table 1. Comparative analysis of tensile properties, strengthening mechanisms, and service temperature regimes for prominent AM metal matrix composite systems.

Matrix System	Al-Based	Ti-Based	Ni-Based	Steel-Based
Typical Reinforcement(s)	TiB_2, TiC	TiB (whiskers), TiC	TiB_2, TiC, ZrB_2	TiC, TiB_2, CNTs
Key Strengthening Mechanisms	Grain refinement (heterogeneous nucleation), load transfer, Zener pinning of grain boundaries and precipitates.	In situ-formed whisker reinforcement, solid solution strengthening (e.g., from C), grain refinement, dislocation hardening from CTE mismatch.	Grain refinement, precipitation hardening (from decomposed reinforcements), formation of serrated grain boundaries, Orowan strengthening by nano-phases.	Stabilization of dislocation cell structures via solute segregation, grain refinement, dispersion strengthening, Hall–Petch strengthening.
Effective Temperature Regime	~250–350 °C	~400–550 °C	~650–900 °C	~20–600 °C
Notable Challenges/Trade-offs	Rapid coarsening of intermetallics >300 °C; detrimental interfacial reactions (e.g., with SiC); common ductility penalty.	Oxidation and phase instability >400 °C in base alloy; complex solidification microstructures; anisotropy from prior -β grains.	Reinforcement decomposition and pore formation; crack sensitivity; requirement for very high densification.	Breakdown of cellular structure >600–700 °C; elemental segregation dynamics; limited data on composite versions at very high T.

Furthermore, the dominant strengthening mechanism strategically shifts with the intended service temperature. For Al- and Ti-based composites targeting medium temperatures (250–550 °C), performance hinges on microstructural stabilization via Zener pinning of grains and precipitates. At higher temperatures (650–900 °C) in Ni-based systems, where diffusion is rapid, grain boundary engineering (e.g., serrated GBs) and nano-scale precipitate hardening become critical for retaining both strength and ductility. In steels, the unique dislocation cell structure inherent to AM provides exceptional room-temperature strength, and reinforcements act primarily to stabilize this metastable structure against recovery.

A critical issue illuminated by this cross-system comparison is the inherent tension between AM-induced anisotropy and the benefit of reinforcement. While reinforcements can disrupt columnar grain growth (e.g., in Ti and Ni alloys), introducing more isotropic equiaxed structures, they can also simultaneously introduce new sources of anisotropy (e.g.,

aligned whisker networks) or act as stress concentrators that exacerbate the detrimental effects of residual porosity or lack-of-fusion defects. The frequently reported "ductility penalty" in AM MMCs, even with strength gains, cannot be attributed solely to classical composite mechanics but is often a convolution of reinforcement distribution, inherited AM defects, and anisotropic matrix microstructure. Studies that report tensile properties solely along the build direction provide an incomplete picture of structural reliability.

Therefore, the landscape of tensile properties in AM MMCs is not merely a catalog of improved strength values. It is a complex interplay where the benefits of reinforcement are modulated, and sometimes compromised, by the idiosyncrasies of the AM process itself. Advancing the field requires a shift towards more comparative, statistically robust studies that (1) systematically vary one key parameter (e.g., reinforcement size, volume fraction) while holding AM parameters constant, (2) report full anisotropic property sets and defect populations, and (3) employ coupled mechanical testing and microstructural quantification to build predictive, rather than descriptive, structure–property relationships. The ultimate goal is to transition from demonstrating feasibility to enabling reliable design.

3. Wear Properties of AM MMCs

Wear is a critical challenge in various industries, impacting the lifespan, reliability, and efficiency of mechanical components. The gradual loss of material due to mechanical interactions between surfaces in relative motion leads to component failure, material degradation, and increased operational costs. This issue is particularly severe in industries such as automotive, aerospace, energy, and manufacturing, where wear resistance, thermal stability, creep resistance, and mechanical strength are essential [119]. The mechanisms behind wear are primarily driven by friction, chemical reactions like oxidation, and physical factors such as applied load and temperature [120]. In extreme service conditions suffering from high-load and temperature, wear mechanisms can be worsened by increased energy input at sliding interfaces, accelerating material degradation and reducing component lifespan. Moreover, wear mechanisms are influenced by oxidation at high temperatures: oxidation-driven wear arises when oxygen reacts with the material's surface, producing oxide layers that can either protect or damage the wear depending on the adhesion and properties of the oxide film [121]. This oxidation can interact with other wear mechanisms such as adhesion and abrasion, where the wear debris from oxidized layers can cause further surface damage, increasing the wear rate [122]. To improve wear resistance, metal matrix composites have emerged as promising materials due to their excellent wear resistance, mainly endowed by the extremely hard reinforcing particles [123]. Figure 10 collates reported COF data across various AM MMC systems, providing a direct visual comparison of their frictional performance. The compilation serves to highlight the general effectiveness of reinforcement in reducing the COF, thereby offering a preliminary performance benchmark across different material categories. However, a comprehensive assessment of wear resistance necessitates the concurrent consideration of wear rates and specific testing conditions.

Essentially, reinforcements enhance surface hardness and oxidation resistance, prolonging component lifespan under severe conditions. Among the complex microstructures in composites, the matrix–reinforcement interaction is crucial in improving wear performance, as the uniform distribution and strong bonding between phases can mitigate the effects of delamination or cracking, which often contribute to wear in conventional metallic materials [124]. Moreover, apart from the typical abrasive wear dominated by matrix deformation, the reinforcements can induce a transformation to more favorable wear modes, such as mild wear or oxidative wear, which reduces the material loss. The hard reinforcements can further limit the plowing effect during sliding contact, where the material

surface is deformed by abrasive particles [125]. Hence, the resulting wear mechanism shift, combined with the increased hardness, provides enhanced wear resistance. Recent advancements in AM of MMCs have revealed significant potential for improving the wear properties of metallic materials. AM technologies such as L-PBF and DED offer precise control over reinforcement dispersion and volume fraction, allowing for the design of composites with optimal wear-resistant properties. Herein, we made a review of the latest studies of AM composites, consisting of five different parts based on various metal systems (Al, Ni, Ti, Fe, and Cu), for an overall demonstration.

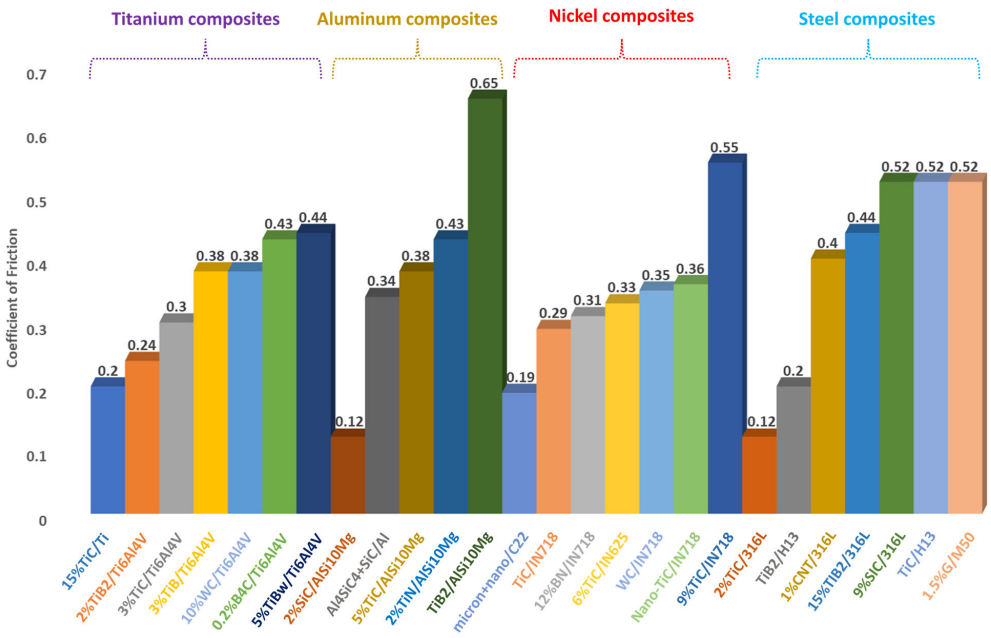


Figure 10. Coefficient of friction of additively manufactured metal matrix composites. (Table S2 in the Supplementary Materials.) [126–148].

3.1. Aluminum Matrix Composites

Traditional manufacturing methods for aluminium matrix composites, such as stir casting, powder metallurgy, spray deposition, and hot extrusion, have limitations, including complex processes, inhomogeneous dispersion, and significant aggregation of nano-reinforcements, which reduce mechanical properties and wear resistance [149]. A promising alternative is the AM technique, which has been explored by several researchers. Xi et al. [143] have reported significant improvements in both mechanical properties and wear resistance with the incorporation of SiC particles into the AlSi10Mg matrix, though the effects are contingent on the SiC content. The findings indicate that wear resistance improves with SiC reinforcement up to 2% content, where the composite achieves a peak wear resistance of 1.84×10^{-3} mm^3/Nm, significantly better than the 4.12×10^{-3} mm^3/Nm observed for pure AM AlSi10Mg. The wear behavior is closely linked to changes in the microstructure caused by SiC reinforcement. SiC particles act as nucleation agents during solidification, promoting heterogeneous nucleation and leading to finer grains, contributing to the increased hardness and wear resistance, as shown in Figure 11a,b. As SiC content increases, the grain morphology changes from columnar dendrites to equiaxed structures, and the secondary dendrites gradually disappear, resulting in a more uniform distribution of phases such as α-Al, Si, and Mg_2Si, as shown in Figure 11c–h. The refinement reduces low-angle grain boundaries, strengthening the material's resistance to surface deformation and wear.

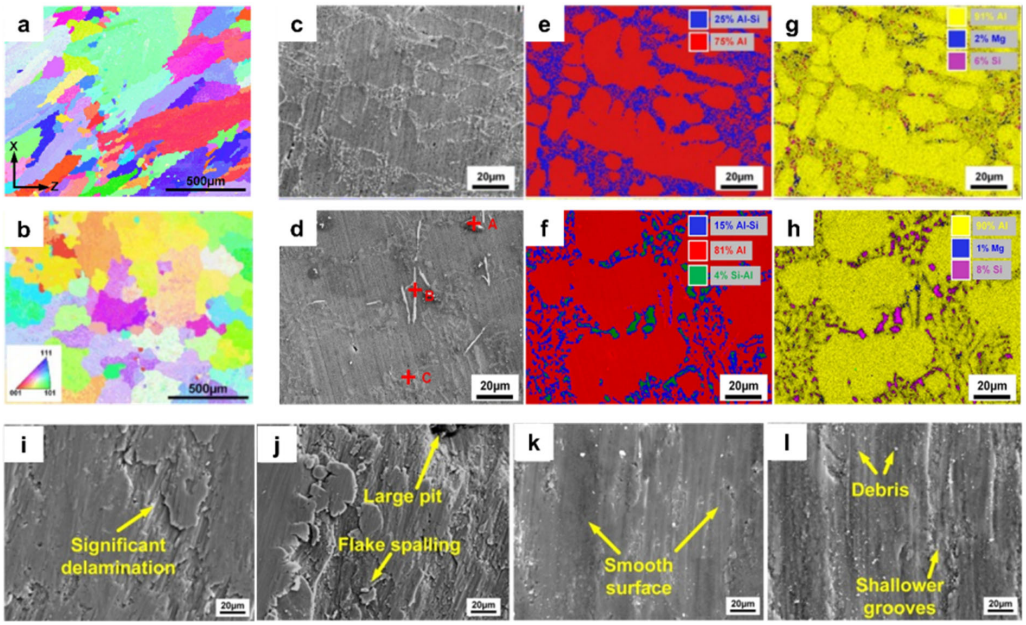


Figure 11. EBSD results of (**a**) AlSi10Mg, (**b**) 2% SiC/AlSi10Mg, (**c**) SEM image of AlSi10Mg, (**d**) 2% SiC/AlSi10Mg, EDS map of the phase distribution and the elements distribution of (**e**) AlSi10Mg, (**f**) 2% SiC/AlSi10Mg. Overlay (**g**) AlSi10Mg, (**h**) 2% SiC/AlSi10Mg. SEM images of worn surfaces of (**i**) AlSi10Mg, (**j**) 1% SiC/AlSi10Mg, (**k**) SEM image of worn surfaces of 2% SiC/AlSi10Mg, (**l**) SEM image of worn surfaces of 3% SiC/AlSi10Mg. Adapted with permission from Ref. [143]. 2020, Elsevier.

The wear mechanisms also strongly depend on the reinforcement content. In the AM bare AlSi10Mg alloy, the worn surface exhibits severe delamination, with visible "stairs" formed by the repeated peeling off of the material under shear stress, as shown in Figure 11i. This is indicative of adhesive wear, where the softer aluminum matrix deforms under friction, and the coarse Si phases contribute to material removal through cutting action. The formation of these delaminations weakens the material over time, leading to increased wear. Remarkably, the addition of SiC particles significantly alters the wear behavior. At 1% SiC, the worn surface shows the formation of shallow grooves, and the surface peeling is reduced, suggesting a shift from adhesive to abrasive wear, as shown in Figure 11j.

The 2% SiC composite exhibits a smooth worn surface with no significant signs of delamination or adhesion, as shown in Figure 11k. This transition is likely due to the increased hardness and the reduced ability of the SiC particles to cut into the material's surface. As a result, the wear resistance is markedly improved, with the material able to resist deformation and surface damage more effectively during repeated friction. At higher SiC contents (3%), the wear resistance begins to deteriorate due to increased porosity and the tendency for second-phase particles to detach from the matrix. This detachment generates deep grooves and increases the wear rate, as shown in Figure 11l.

Further improvements in wear resistance have been demonstrated by Gu et al. [134] in L-PBF TiC reinforcement AlSi10Mg nanocomposites, with densification exceeding 98% of the theoretical density. This optimal densification leads to significant improvements in wear resistance, with a low COF of 0.38 and a wear rate of 2.76×10^{-5} mm^3 N^{-1} m^{-1}, respectively. The key to this enhancement lies in the uniform distribution of nanoscale TiC particles within the AlSi10Mg matrix. The TiC nanoparticles, finely dispersed throughout the matrix, help to distribute applied stresses more evenly during wear tests, minimizing the formation of cracks and reducing material degradation, as shown in Figure 12a–d. The TiC

nanoparticles also contribute to strain-hardening during sliding friction, forming a durable tribolayer that further improves wear properties, as shown in Figure 12f. Importantly, an inferior densification with lower input energy causes pores and non-homogeneous TiC dispersion, as shown in Figure 12e. These microstructural inhomogeneities result in localized stress concentrations that promote crack formation and surface wear, leading to a higher COF (0.63) and wear rate (7.46×10^{-5} mm^3 N^{-1} m^{-1}), respectively. Hence, the uniform distribution of reinforcement may be crucial for enhanced wear resistance of AM Al matrix composites. Further optimization of the wear resistance by controlling the size of reinforcing particles may be essential, as nanoparticles could generally contribute to smoother frictional behavior by promoting the formation of protective tribofilms or oxide layers at the wear surface, reducing direct contact between the matrix and the counter-surface, as shown in Figure 12g,h.

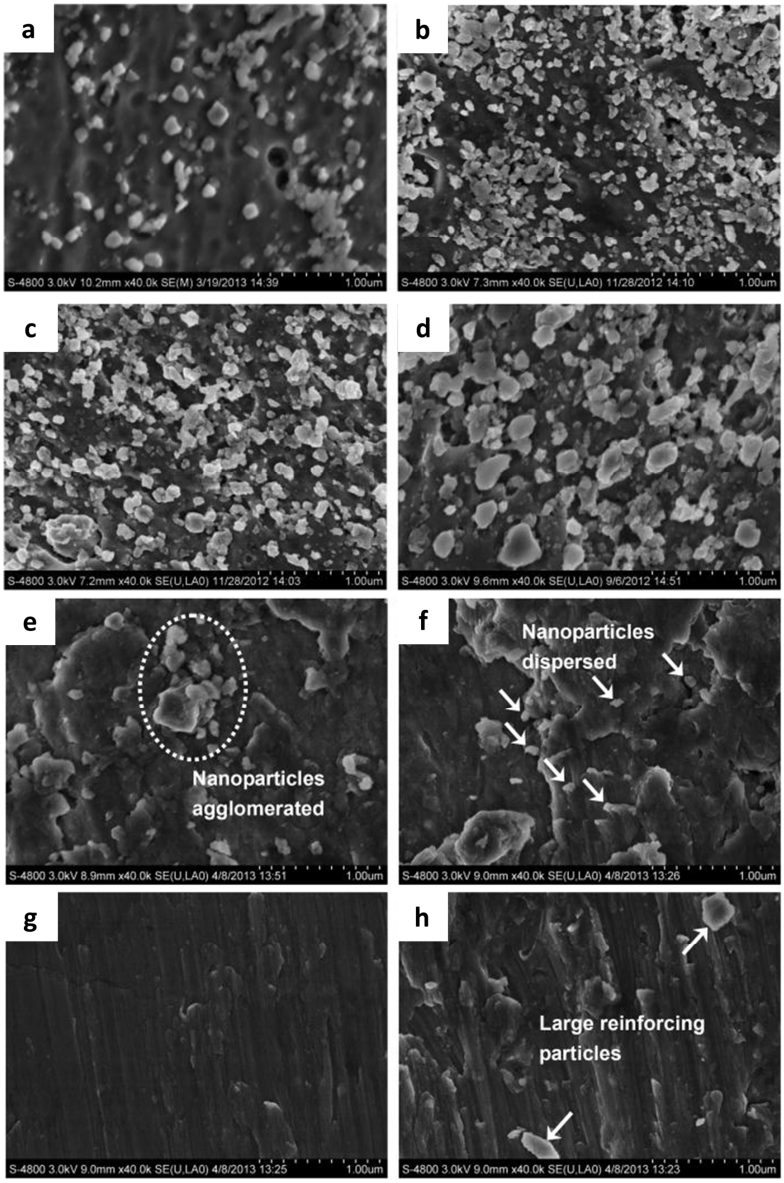


Figure 12. High-magnification FE-SEM images showing characteristic morphologies of TiC reinforcement in SLM-processed TiC/AlSi10Mg parts at different LEPULs: (**a**) 250 J/m; (**b**) 500 J/m; (**c**) 700 J/m; (**d**) 1000 J/m. FE-SEM images showing characteristic morphologies of worn surfaces of SLM-processed TiC/AlSi10Mg nanocomposite parts using various LEPULs: (**e**) 250 J/m; (**f**) 500 J/m; (**g**) 700 J/m; (**h**) 1000 J/m. Reprinted from Ref. [134].

In summary, the wear resistance of AM Al composites is critically dependent on achieving a uniform dispersion of nano-reinforcements (SiC, TiC), which shifts the wear mechanism from severe adhesion/delamination to milder abrasion or oxidation. The optimal reinforcement content is low (often 1–2 vol%), beyond which agglomeration and defect formation become detrimental. This underscores a central theme: the benefits of reinforcement are fully realized only within a narrow window of near-full densification and perfect dispersion. The process parameters, therefore, are as critical as the material selection itself in determining tribological performance.

3.2. Titanium-Based Composites

Wear resistance is a critical property for titanium and its alloys, particularly in applications involving high-stress environments such as aerospace, biomedical implants, and automotive components [150]. Despite titanium's excellent strength-to-weight ratio, corrosion resistance, and high-temperature stability, its wear performance can be compromised in certain conditions. Titanium's relatively low hardness, especially in the case of pure titanium, makes it susceptible to abrasive and adhesive wear when exposed to rough contact surfaces or high sliding velocities [151]. This is particularly problematic in engineering applications where surface degradation can compromise the material's functionality and longevity. To mitigate wear issues, alloying and surface modification techniques, such as the incorporation of hard phases, coatings, and surface treatments (e.g., anodizing, nitriding), are commonly employed to enhance its wear resistance [152]. The formation of protective oxide films on the titanium's surface also plays a role in reducing wear by acting as a barrier between the material and the wear counterpart [153]. Additionally, research into TMCs reinforced with hard particles has shown promise in improving wear properties, which significantly improves the material's hardness and wear resistance. Understanding and addressing the wear behavior of TMCs, especially for the fast-growing AM Ti matrix composites, is essential for ensuring their durability and performance in demanding applications [154].

One way to improve the wear-resistance of Ti alloys is to facilitate in situ reaction between reinforcements and the Ti matrix during AM. Patil et al. [140] reported that the incorporation of 2% TiB_2 into Ti64 alloys processed via Direct Metal Laser Sintering (DMLS) significantly improved the wear resistance of the base alloy. The chemical reaction between TiB_2 and Ti forms nanosized TiB whiskers, which are distributed throughout the titanium matrix, as shown in Figure 13a,b. In the base Ti-6Al-4V alloy, wear is driven by delamination and spalling, which results in material loss, as shown in Figure 13c. However, in the modified alloy, the in situ-formed TiB whiskers reduce plastic deformation, leading to a more uniform wear pattern with minimal material loss, as shown in Figure 13d. The presence of TiB whiskers also hindered the growth of large grains, further improving the alloy's resistance to plastic deformation. Notably, the strong interfacial bonding between the TiB whiskers and the titanium matrix distributes stresses across the alloy, enhancing wear resistance and preventing the detachment of wear debris. Alternatively, Chao et al. [129] found that the addition of 3% TiB_2 to the L-PBF-processed Ti64 alloy also significantly improved wear performance, with wear loss in the bare alloy approximately double that of the composites, indicating a considerable enhancement in wear resistance. The improvement is attributed to the transformation of TiB_2 particles into needle-like nanoscale TiB phases during the L-PBF process. Figure 13e illustrates that the solidification pathway during L-PBF proceeds as TiB_2 + Ti-6Al-4V $\rightarrow$ L $\rightarrow$ TiB + βTi $\rightarrow$ TiB + βTi + αTi, leading to the formation of needle-like TiB reinforcements that measure 0.5–1 μm in length and less than 100 nm in width, as shown in Figure 13f. This results in the L-PBF composites with a nano hardness of 6 GPa, much higher than traditional sintered counterparts

(~4.4 GPa), as shown in Figure 13g. These nanoscale TiB and the grain refinement caused by strong pinning of grain boundaries by TiB significantly increase the hardness of L-PBF Ti matrix composites, which reduces dislocation density and prevents crack propagation upon wear. Remarkably, the wear mass loss of the L-PBF composites was also lower than that of counterparts made by HIP, owing to the superior microstructure refinement and surface hardness provided by the L-PBF process. The employment of in situ reaction between TiB_2 and Ti matrix to enhance wear resistance of AM Ti matrix composites seems to be general. Zhao et al. [146] revealed that the 5% TiBw-reinforced Ti6Al4V achieved by L-PBF of TiB_2-Ti composites showed a significant improvement in wear resistance. The COF for the TiB whisker/Ti6Al4V composite was 0.44, significantly lower than the 0.83 observed for the bare L-PBF Ti6Al4V alloy. The presence of an in situ-synthesized nanoscale TiB whisker network and residual TiB_2 hard particles contributed to increased shear deformation resistance in the composite, which directly led to higher hardness and the lower COF.

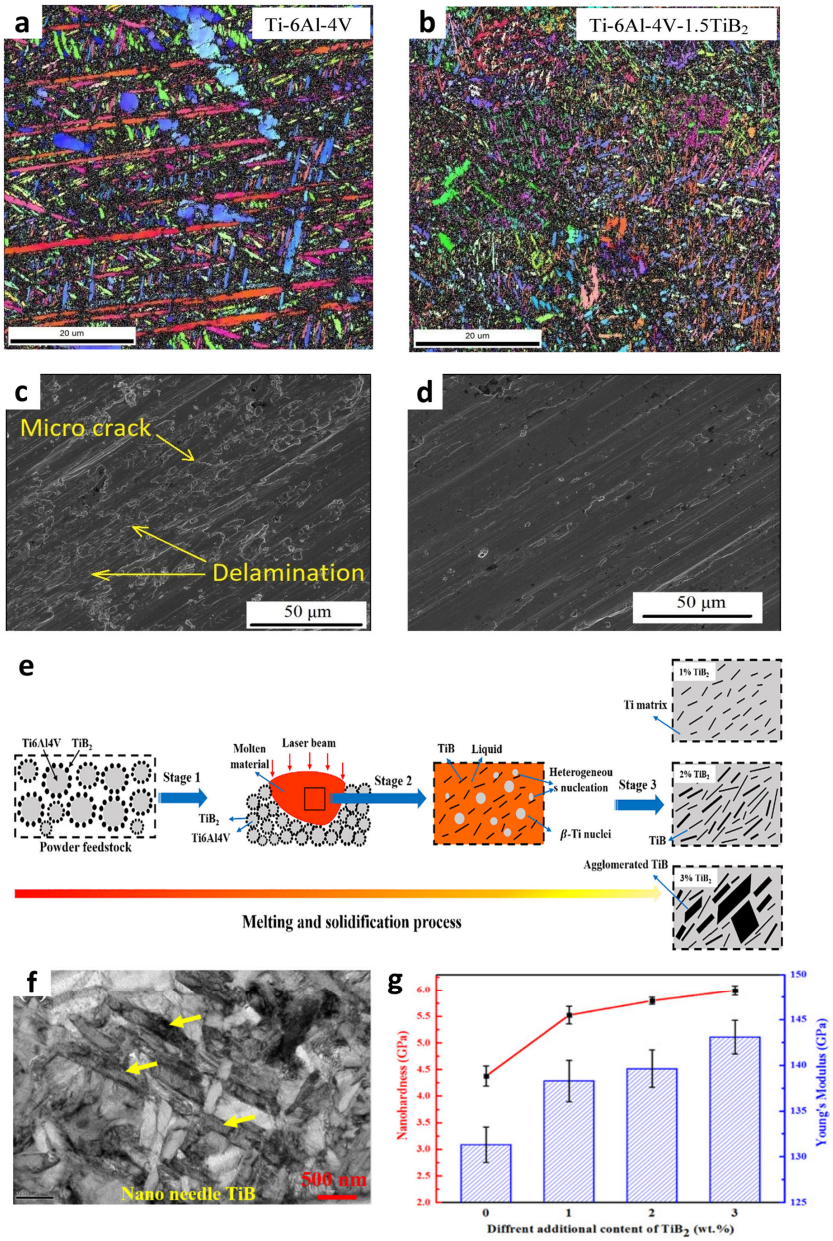


Figure 13. IPF maps of (**a**) Ti-6Al-4V alloy, (**b**) 1.5% TiB/Ti-6Al-4V. SEM images of worn surfaces after wear testing of (**c**) Ti-6Al-4V alloy and (**d**) TiB_2/Ti-6Al-4V (**f**) high-magnification dark-field micrograph

of TMC. Adapted with permission from Ref. [140]. 2019, Elsevier. (**e**) The schematic illustration of the formation mechanism for the TiB/Ti-6Al-4V composites. The mixture of TiB and Ti-6Al-4V powders melted into the liquid phase, stage 2: primary β-Ti nucleated and grew from the liquid phase, stage 3: a surface tension gradient and Marangoni flow accelerating the rearrangement of precipitated TiB phase and generating the mutual parallel strips microstructure. (**g**) Calculated nano hardness (H_d) and Young's modulus (E) values of samples with different TiB reinforcement. Adapted with permission from Ref. [129]. 2019, Elsevier.

The microstructure "self-evolution" of the reinforcements without chemical reaction with the Ti matrix is another way to improve wear resistance. As demonstrated by Tang et al. [142] in a 3% TiC-reinforced Ti-6Al-4V processed by L-PBF, the composite exhibited a significant enhancement in wear properties attributed to its unique microstructure. Tribological testing revealed excellent wear resistance, with a friction coefficient of 0.303 and a wear rate of 1.221 $mm^3/m{\cdot}N$ under a 15 N applied load. These properties were superior to those of L-PBF Ti-6Al-4V, due to the presence of nanoscale eutectic TiC phases and the formation of a carbon-enriched solid lubricant film that reduced friction and wear, as shown in Figure 14a,b. The structure of the reinforcements was primarily reshaped by the L-PBF processing, where nanoscale eutectic TiC phases, less than 95 nm in thickness, were present—this is a characteristic not typically observed in TiC/Ti64 matrix composites, as shown in Figure 14c,d. These nanoscale TiC phases were rationalized by the dissolution–reprecipitation process in the extremely high temperature during L-PBF, and are key contributors to the enhanced wear-resistance properties.

Importantly, the properties of the AM Ti matrix composites were influenced by the processing parameters. For example, in L-PBF TiC-Ti composite, increasing the laser power raised the energy density, leading to greater dissolution of TiC particles and an increased content of eutectic TiC phases, as shown in Figure 14e–j [133]. However, this also reduced the cooling rate, resulting in larger grain sizes and fewer low-angle grain boundaries (LAGBs). Conversely, increasing the laser scanning speed decreased energy density, improving the solidification rate and producing smaller grains and more LAGBs. These microstructural differences at various energy density inputs lead to different wear-resistance properties. Moreover, for L-PBF TiB whisker/Ti6Al4V composites with TiB_2 reinforcement as a precursor, at lower energy densities (E = 60 J/mm^3), the composite exhibited a matrix primarily composed of nano-scale TiB whiskers with a B27 structure and partially unmelted micro-scale TiB_2 particles with a hexagonal structure [146]. As the energy density increased, the morphology of TiB whisker transitioned from acicular to rod-like or plate-like, and the TiB network expanded or may even have broken apart, Figure 14k–p. This structural evolution was influenced by the molten pool's flow behavior during L-PBF, which affected the distribution and formation of the TiB reinforcements. As the energy density increases, the network structure and morphology of TiB are further optimized, contributing to improved tribological behavior.

In conclusion, wear resistance in AM Ti composites is enhanced not merely by adding hard phases, but by leveraging the AM process to create in situ solid lubricant films (from TiC) and interconnected reinforcement networks (TiB). The wear mechanism transitions from abrasive/adhesive to a more protective mode. A key finding is the "self-evolution" of reinforcements during processing, where laser parameters dictate the final morphology and distribution, directly governing tribological efficacy. This highlights the intricate link between AM energy input, microstructural evolution, and surface performance in Ti systems.

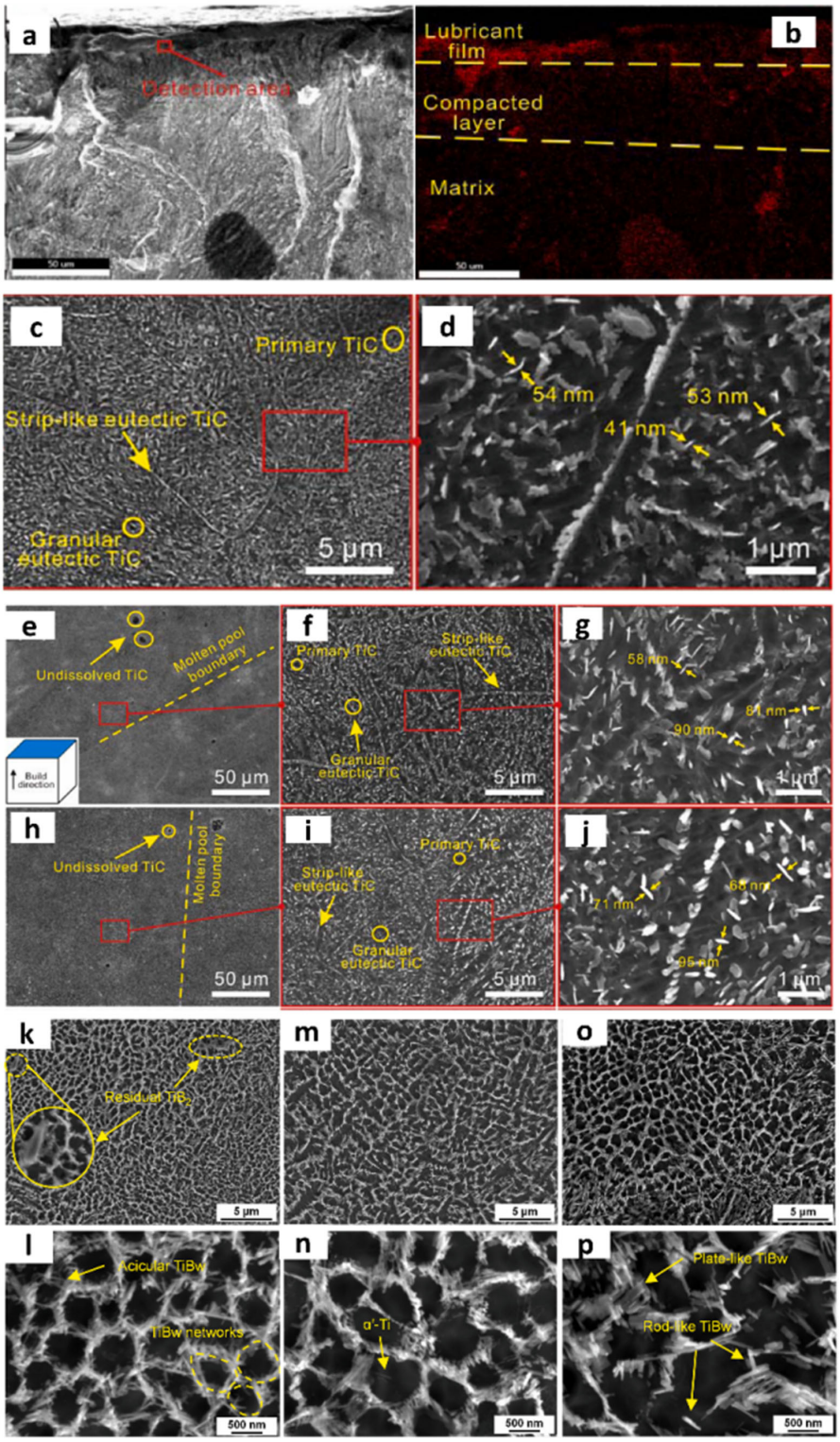


Figure 14. (**a**,**b**) SEM image and elemental distribution of cross-section of worn scar of the TiC/Ti6Al4V (laser power of 240 W, laser scanning speed of 1000 mm/s) after tribological test at 15 N. (**c**,**d**) SEM image of microstructures of the SLM-processed TiC/Ti6Al4V obtained from side view, laser power of 200 W, laser scanning speed of 1200 mm/s. SEM image of microstructures of the SLM-processed composites obtained from top view: (**e**–**g**) laser power of 200 W, laser scanning speed of 1000 mm/s; (**h**–**j**) laser power of 240 W, laser scanning speed of 1000 mm/s. Cross-sectional microstructure of TMC samples fabricated by SLM under different energy densities: (**k**,**l**) E = 60 J/mm^3, TMC1; (**m**,**n**) E = 110 J/mm^3, TMC2; (**o**,**p**) E = 160 J/mm^3, TMC3. Adapted with permission from Ref. [146]. 2023, Elsevier.

3.3. Nickel-Based Composites

To enhance the wear resistance and mechanical properties of nickel-based superalloys, nickel alloys are often reinforced with ceramics such as borides, carbides, and nitrides. Recent advancements in nanotechnology have highlighted the potential of nano-reinforcements, significantly improving strength, microhardness, and wear resistance. However, both the reinforcement-induced microstructural evolution and the sample quality have pronounced influences on the wear resistance of AM Ni-based composites. Firstly, the defect-lean nature seems to be the primary factor for the enhanced wear properties. Jia et al. [136] found that the wear and strengthening mechanisms of L-PBF TiC-reinforced Inconel 718 composites are governed by laser energy density, which determines the densification behavior. At lower volumetric laser energy densities (3.0–3.9 kJ/mm^3), inadequate densification results in high surface roughness and material delamination, leading to severe adhesive wear, as shown in Figure 15a,b. The COF fluctuates due to unstable wear debris adhesion, while the wear rate remains high. As the volumetric laser energy density increases to 4.7 kJ/mm^3, densification improves, reducing plastic deformation and shifting the dominant wear mechanism to mild abrasive wear. At the optimal energy density of 5.1 kJ/mm^3, near-full densification is achieved, and the microstructure also becomes highly refined with a uniform dispersion of TiC reinforcements, leading to the lowest COF (0.29) and wear rate (2.69 $\times$ 10^{-4} mm^3 N^{-1} m^{-1}), as shown in Figure 15c,d. Moreover, the TiC reinforcements change the microstructure of the as-built Ni-based alloys. They controlled the melt pool solidification by acting as heterogeneous inoculants to promote refined grain structures and disrupt columnar dendritic growth. The particles also act as a hard supporting network, reducing material removal and mitigating counter-face ball abrasion. The combination of these microstructural benefits enhance hardness and wear resistance of the L-PBF TiC-In718 nanocomposites. This enhanced wear performance and the associated mechanisms are found to be applicable for other AM In718 composites with various reinforcements.

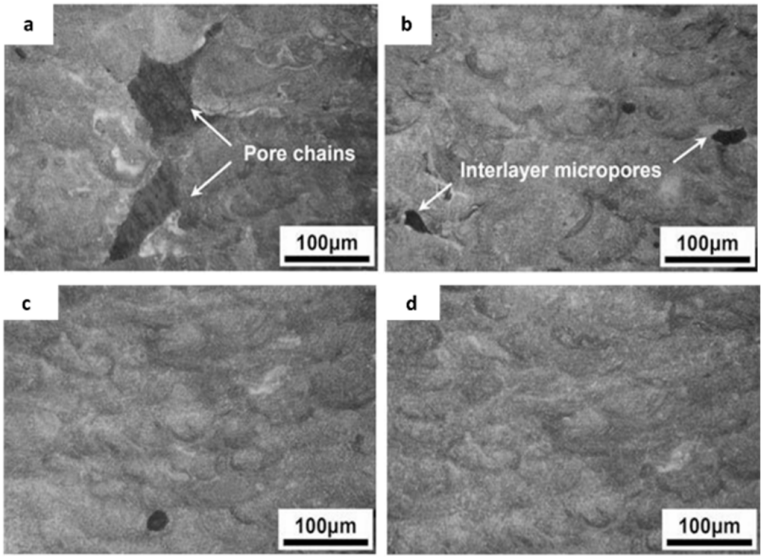


Figure 15. Optical microscopy images showing interlayer microstructures under different SLM conditions: (**a**) 3 kJ/mm^3; (**b**) 3.9 kJ/mm^3; (**c**) 4.7 kJ/mm^3; (**d**) 5.1 kJ/mm^3. Adapted with permission from Ref. [136]. 2014, Springer Nature.

Except for the widely adopted AM Ni-based materials, In718, the Hastelloy C22 is another nickel-based superalloy known for its excellent corrosion and oxidation resistance due to its high Ni-Cr-Mo content, which can contribute to solid solution strengthening in γ-FCC

phase. These properties make it widely used in the chemical and marine industries. Yang et al. [144] investigated high-wear-resistant nickel-based composites using DED by incorporating nano- and micron-sized WC particles into the Hastelloy C22 matrix. The research compared three kinds of composite coatings: 12% nano-WC/C22, 12% micron-WC/C22, and a hybrid (6% nano-WC + 6% micron)-WC/C22. Due to the rapid solidification process, grain morphology evolved from planar to equiaxed structures, influenced by the thermal gradient (G) and solidification rate (R). At high G/R ratios near the coating–substrate interface, planar solidification occurred, while a decrease in this ratio promoted dendritic grain formation and eventual transition to equiaxed structures due to enhanced supercooling upon DED, as shown in Figure 16a–c. The bare DED C22 mainly consisted of M_6C and γ-Ni solid solution. After the incorporation of WC reinforcements, the primary phases in the DED WC-reinforced C22 composites were identified as γ-Ni and carbides (such as M_6C, WC, W_2C, and $M_{12}C$), as shown in Figure 16d. These carbides are mainly distributed at grain boundaries, contributing to further grain refinement of as-built composites and extra strengthening via load-bearing. Remarkably, the nano-/micron-WC/C22 composite coating exhibited the most significant refinement, resulting in superior hardness and wear resistance, as shown in Figure 16e, showing a 92.3% reduction in mass loss compared to the C22 coating, as shown in Figure 16f. These improvements were attributed to the unique hybrid reinforcement structure. During DED, partial dissolution of micron-WC particles occurs, increasing the carbon content and contributing to solid solution strengthening. Simultaneously, the nano-WC particles completely dissolved under high-energy laser irradiation, leading to the uniform formation of carbides that impeded dislocation movement and enhanced structural integrity.

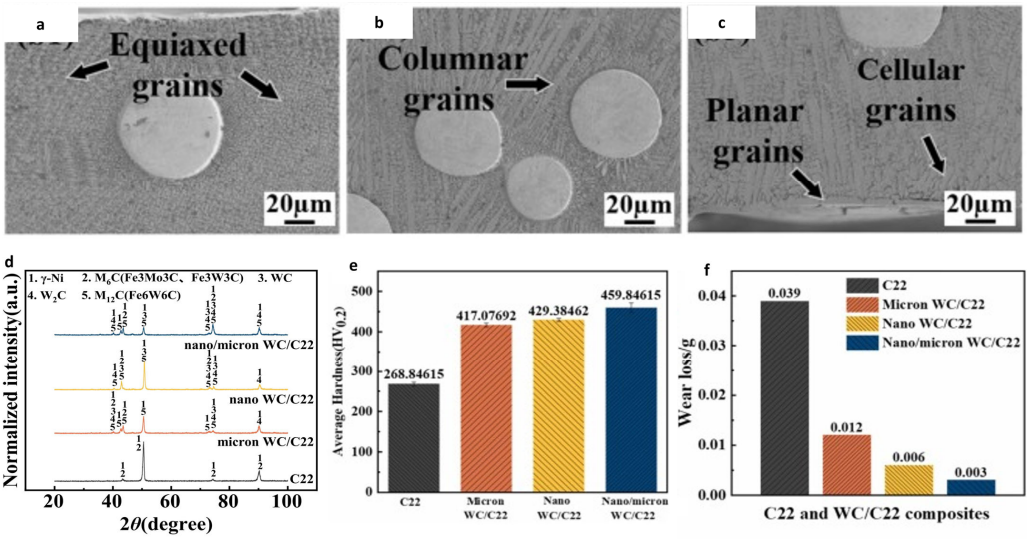


Figure 16. Evolution of microstructural morphology: (**a**–**c**) micron-WC/C22 composite coating. (**d**) XRD patterns of C22 and WC/C22 composite coatings. (**e**) Curve of friction coefficient; (**f**) mass loss. Adapted with permission from Ref. [144]. 2024, Elsevier.

These microstructural tuning behaviors led to several mechanisms that contributed to the enhanced wear resistance of hybrid reinforcement. First, grain refinement and carbide distribution played a critical role. The localized carbides can pin grain boundaries during the thermal cycles upon AM and restricted grain coarsening. This can be demonstrated by the most refined microstructure of hybrid composites among all three comparison samples, as shown in Figure 17a. Second, the increased microhardness allowed the coatings to withstand higher loads, reducing penetration and plastic deformation during wear. Post-mortem microstructural analysis reveals that the residual micron-WC particles protruded during wear, supporting the mechanical support behavior and minimizing coating spalling,

as shown in Figure 17b–e. Third, the dispersed carbides could impede crack propagation, further reducing wear-induced degradation. The DED C22 matrix mainly produced large, flaky debris with visible fatigue cracks (a phenomenon associated with severe adhesive wear), as shown in Figure 17f,g; yet, the DED nano-/micron-WC/C22 composite generated fine, powder-like debris, confirming superior crack resistance and minimal material removal, as shown in Figure 17h,i. The reduction in wear depth and width further validated the strengthening effects of WC reinforcement. This complex phase transformation of reinforcement, such as the particle/full dissolution of reinforcing elements as well as their subsequent reaction with the Ni matrix, opens new pathways to achieve Ni matrix composites with excellent wear-resistance properties, as shown in Figure 17j.

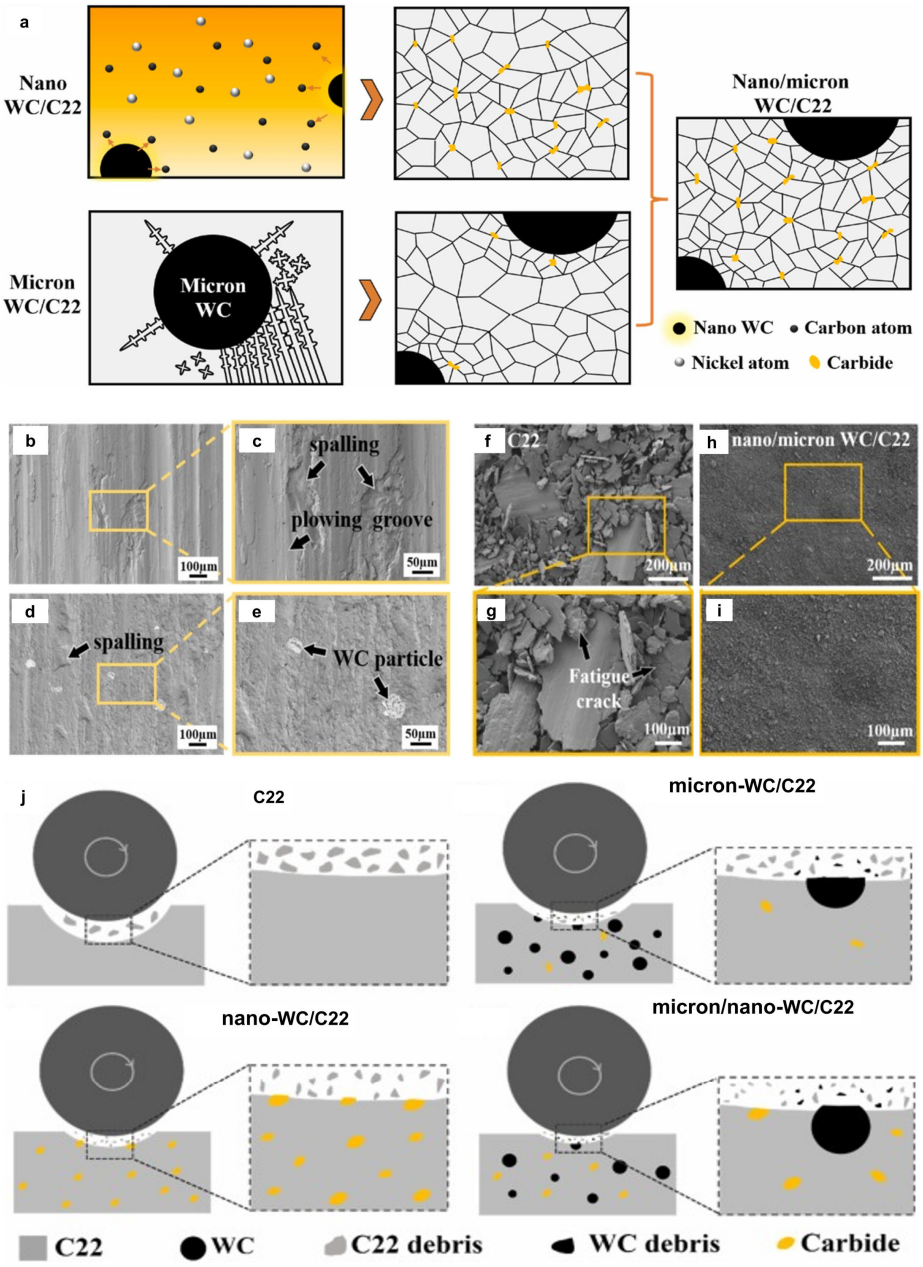


Figure 17. (**a**) Schematic diagram of fine-grain strengthening. Surface morphology of worn coating: (**b**,**c**) C22, (**d**,**e**) nano-/micron-WC/C22. Morphology of worn debris. (**f**,**g**) C22, (**h**,**i**) nano-/micron-WC/C22. (**j**) Schematic diagram of wear mechanism for C22, micron-WC/C22, nano-WC/C22, and nano-/micron-WC/C22. Adapted with permission from Ref. [144]. 2024, Elsevier.

To summarize, the exceptional wear resistance of AM Ni-based composites is achieved through microstructural densification, grain refinement, and the strategic use of reinforcements that undergo in situ transformations to form hard, nano-dispersed precipitates. Hybrid nano-/micron reinforcements (e.g., WC) are particularly effective, combining direct load-bearing with solid-solution strengthening. Crucially, the wear mechanism shifts from severe adhesive wear with macro-delamination to mild wear with fine debris. This transformation is, however, entirely contingent upon achieving near-full density, reiterating that defect control is the non-negotiable prerequisite for superior wear performance in these systems.

3.4. Steel-Based Composites

In recent years, the strength and hardness of 316L stainless steel alloy have proven insufficient for demanding applications in industries such as national defense and nuclear power. These sectors require materials that can withstand heavy loads and offer high wear resistance, especially in extreme conditions. While 316L SS is widely used in energy industries like nuclear and oil and gas for its mechanical properties and corrosion resistance. However, its relatively low strength and wear resistance at high temperatures limit its performance in extreme environments. Despite challenges related to their strength and wear resistance at high temperatures, the incorporation of reinforcing particles significantly improves the wear resistance of the composite, making it a potential solution for high-performance applications.

Firstly, the incorporation of reinforcing particles is found to alter the nanostructures of alloys in the as-built state, which, in turn, influences the wear-resistance behaviors. The wear properties of 2% TiC-reinforced 316L stainless steel alloy by L-PBF were investigated by Zhao et al. [147]. The addition of 2 wt% TiC under optimized process parameters resulted in a 12.4% increase in the average microhardness of the composites, and the average friction coefficient of the composite was reduced remarkably from 0.37 to 0.12. During the melting process, TiC particles acted as nucleation centers due to the high melting point of TiC, hindering crystal cell growth and promoting the formation of the austenite phase. The higher thermal conductivity of TiC (~30 W/m·K) compared to 316Lss (15 W/m·K) also accelerated the cooling and solidification during the L-PBF process. Additionally, the significant difference in thermal expansion coefficients between TiC (7.74×10^{-6}/K) and 316LSS (17.3×10^{-6}/K) increased dislocation density in the as-built composites, enhancing the hardness of the composite based on the typical Taylor strengthening. These combined microstructural tuning effects, including a fine and equiaxed microstructure and enhanced dislocation density, significantly improve the wear resistance of L-PBF TiC-316LSS composites, as shown in Figure 18a–d. Moreover, the incorporation of carbon nanotubes (CNTs) in L-PBF 316LSS also demonstrates a strong modification of the matrix's nanostructures [145]. The cell spacing or size in AM 316L SS is ~400 nm. In comparison, the L-PBF 1% CNT/316L showed ultrafine cellular/columnar structures with short secondary dendritic arms of ~219 $\pm$ 37 nm developed (i.e., a transition of the solidification mode from cellular to dendritic mode occurs), as shown in Figure 18e. This modification of the dislocation cell structure is mainly associated with the carbon segregation along the cellular walls, as shown in Figure 18f–h. It is known that the solidified microstructures are determined by the temperature gradient (G) and growth rate R of the solid–liquid interface, where the value of G/R determines the solidification mode and microstructure. Compared to L-PBF 316LSS, constitutional supercooling of the composites may be different due to carbon segregation, which could influence the growth rate of the solidification front, leading to the transformation of the solidification mode. Simultaneously, the segregation of carbon along cellular boundaries in the L-PBF CNT/316L composite might

increase the boundary strengthening coefficient (k value in the Hall–Petch relationship, $\sigma = \sigma_0 + kd^{-1/2}$, where σ_0 is the lattice friction stress and d is the average grain size). Because of the enhanced dislocation pinning at grain boundaries, the strengthening coefficient of L-PBF 1%CNT/316L composite was calculated to be 499 MPa $\sqrt{\mu m}$, significantly surpassing that of L-PBF 316LSS without CNT modification (~253 MPa $\sqrt{\mu m}$) [155]. The combined effect of cellular structure modification and enhanced dislocation pinning at the cell boundaries endows superior wear resistance of L-PBF 1% CNT/316LSS than AM316L. And a 3–10 times lower wear rate was observed for the composites, depending on the loading conditions.

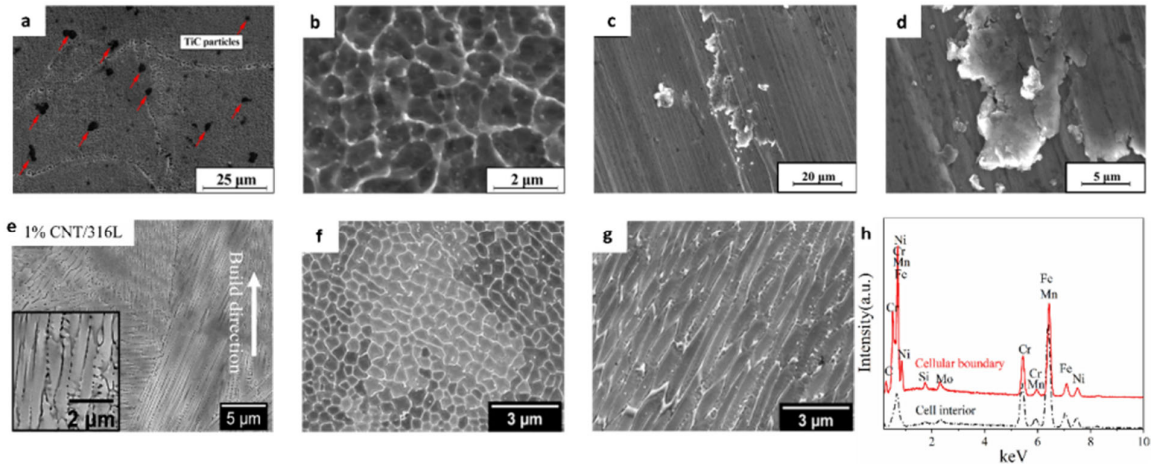


Figure 18. (**a**,**b**) SEM micrographs of the 2% TiC/316LSS composites. (**c**,**d**) SEM images showing the typical worn morphologies of TiC/316L composites. Reprinted from Ref. [147]. (**e**) SEM images of etched surfaces showing sub-grain structure of AM 1% CNT/316L composites. SEM images of under-etched surfaces show C segregation on cellular boundaries of 1% CNT/316L composite (**f**) cellular structure; (**g**) columnar structure; (**h**) EDS spectrum of the cell interior and cellular boundary. Adapted with permission from Ref. [145]. 2022, Elsevier.

The in situ fragmentation of reinforcement during AM provides another way for enhancing wear-resistance. Zou et al. [148] demonstrated a significant improvement in wear resistance of L-PBF SiC-reinforced 316L stainless steel alloys. The 9 vol% SiC-reinforced MMC exhibited a wear rate of 0.77×10^{-5} mm^3/Nm, notably lower than that of the unreinforced 316L alloy. Remarkably, the initially micron-sized SiC particles were reduced to nanoscale dimensions (~150 nm) after laser processing, as shown in Figure 19a,b. This caused significant microstructural changes, including the refinement of the grain structure in the 316L matrix and the formation of a <001> preferred crystallographic orientation with an increment in high-angle grain boundaries (HAGBs), as shown in Figure 19c–h. The wear mechanism of the L-PBF SiC-reinforced 316L composite was influenced by the enhanced microstructure and the presence of SiC particles. Initially, during sliding wear, the wear debris plowed the 316L surface, creating grooves, as shown in Figure 19i. However, as the sliding process continued, the wear debris accumulated and became further deformed. The SiC particles helped resist material deformation by acting as hard reinforcements, transferring the load away from the softer 316L matrix. Additionally, the SiC particles impeded dislocation movement, leading to the formation of a strain-hardened tribolayer on the friction surface, as shown in Figure 19j. This tribolayer further reduced friction and wear, thereby enhancing the overall wear resistance of the AM composites. Thus, the improved tribological performance of the composites can be attributed to the combined effects of enhanced hardness, the support provided by the nanosized SiC hard skeleton, and the strain-hardening mechanism facilitated by the in situ fragmented SiC particles.

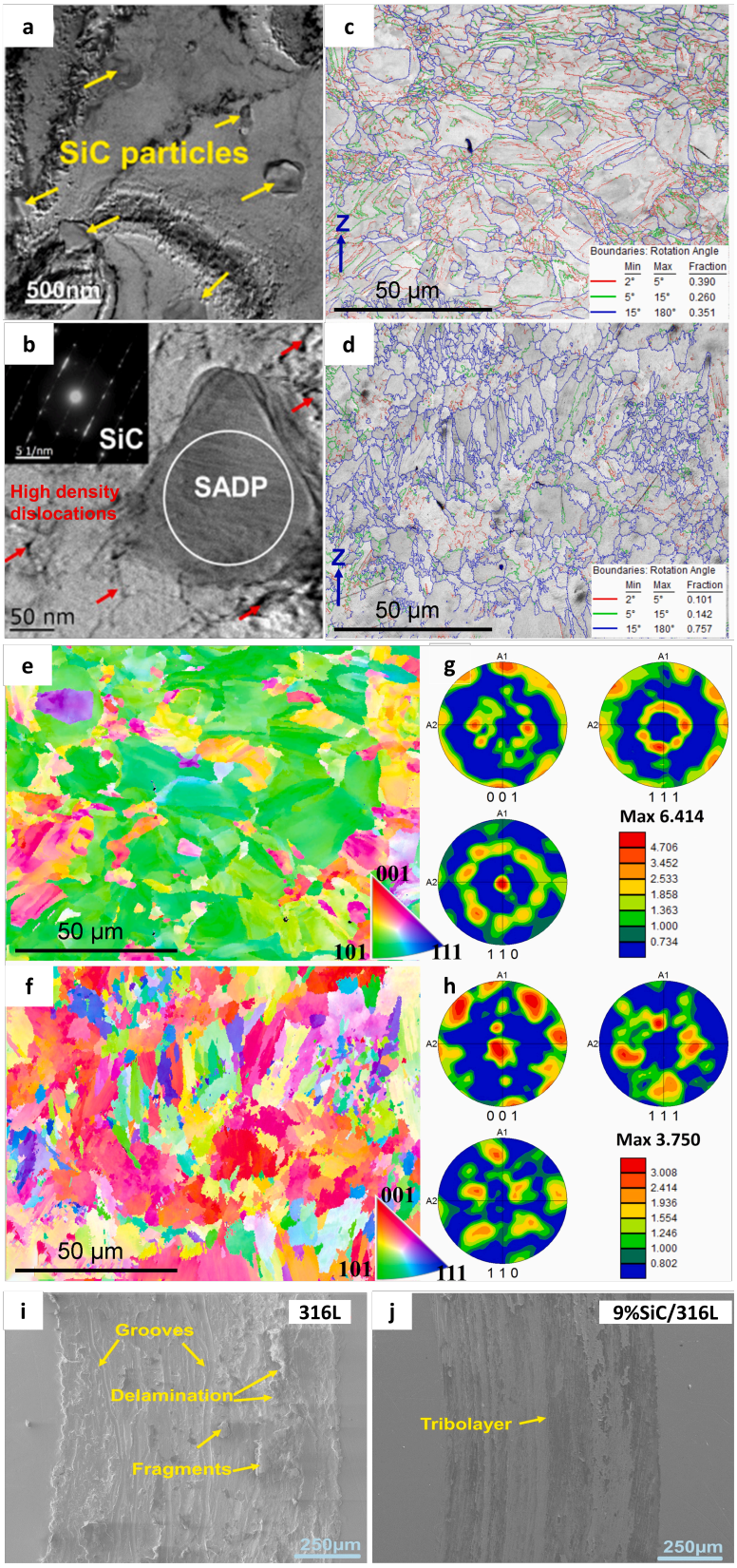


Figure 19. (**a**) Bright-field TEM image of the L-PBF-fabricated S6 MMC showing SiC particles (indicated by yellow arrows). (**b**) Bright-field TEM image showing high dislocation density (highlighted by red arrows) around a SiC particle; the inset shows the corresponding selected area diffraction pattern (SADP). EBSD analysis of the L-PBF-fabricated 316L and MMC (along build direction): (**c**) grain boundary map of 316L; (**d**) grain boundary map of 9%SiC/316L. (**e**) Inverse pole figure (IPF) coloring map of 316L; (**f**) IPF map of 9%SiC/316L. (**g**) Pole figures (PFs) of 316L; (**h**) PFs of 9%SiC/316L. SEM images of L-PBF-fabricated: (**i**) 316L, (**j**) 9%SiC/316L.

Except for the widely studied L-PBF 316LSS, the other AM steels also show wear-resistance superiorities via the composite strategy. AlMangour et al. [127] investigated the wear behavior of a 50 nm TiC-reinforced H13 steel alloy via L-PBF, with results demonstrating superior performance compared to unreinforced H13 steel. The fast cooling rendered by L-PBF leads to a strong and complete martensite corresponding to an α-Fe phase with a BCC crystal structure, and inhibits the grain growth of the TiC nanoparticles because of insufficient time for grain coarsening, remaining as the favorable nanostructured TiC reinforcement after AM. More importantly, TiC nanoparticles were uniformly distributed in the H13 matrix, in an interconnected distribution manner, attributed to the strong convection caused by the rapid heating and solidification, as shown in Figure 20a. The COF of the 15 vol.% TiC/H13 nanocomposites was 0.52, lower than that of pure H13 steel. Additionally, the wear rate of the TiC/H13 nanocomposites was 3.623×10^{-6}, a 26% reduction compared to the wear rate of unreinforced H13 steel (4.906×10^{-6}). The wear mechanism of the TiC-reinforced nanocomposites differed notably from that of unreinforced H13 steel. While the wear of pure H13 steel involved material removal through abrasive micro-cutting, the TiC-reinforced nanocomposites exhibited a strain-hardened tribolayer, characterized by shallower grooves and fewer abrasive fragments, as shown in Figure 20b. This change in the wear mechanism contributed to the reduced wear volume. Further analysis of the worn surfaces revealed that both pure H13 alloy and TiC/H13 nanocomposites exhibited predominance of iron, carbon, and chromium. However, the TiC/H13 nanocomposites showed less carbon, indicating minimal loss of TiC during wear. TiC particles were observed on the worn surface, providing additional protection to the matrix. The absence of particle cracking or detachment, combined with the increased hardness and strain-hardened tribolayer, suggests a significant enhancement in wear resistance.

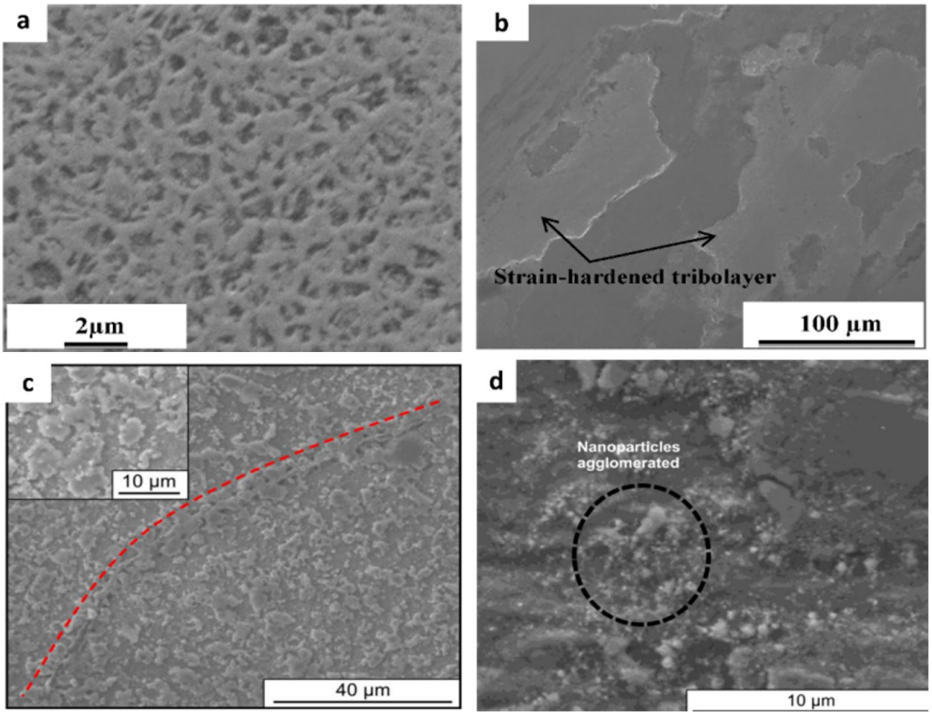


Figure 20. (**a**) TiC/H13 nanocomposite interconnected distribution. (**b**) SEM images showing morphologies of the worn surfaces of the nanocomposites TiC/H13 (**c**) after HIP treatment. The inset in the upper-left corner shows particle agglomerations after HIP treatment. Adapted with permission from Ref. [127]. 2016, Elsevier. (**d**) SEM images showing morphologies of the worn surfaces of the nanocomposites TiB_2/H13 after HIP treatment. Adapted with permission from Ref. [128]. 2017, Elsevier.

Post-heat treatment could play a vital role in the wear resistance of AM steel matrix composites. For instance, nano-TiB_2-reinforced H13 steel made by L-PBF exhibited a wear rate of approximately 1.268×10^{-6} mm^3/Nm, with an average COF of 0.209, both of which are notably lower than those of untreated L-PBF H13 steel. These significant improvements in wear resistance were attributed to the formation of a strain-hardened tribolayer, which was more prominent in the nanocomposite due to the homogeneous dispersion of TiB_2 nanoparticles within the H13 steel matrix. After hot isostatic pressing (HIP) post-treatment, major pores were eliminated, and the grains were transformed into intermittent structures with crystalline clusters, as shown in Figure 20c. However, this process led to slight grain coarsening and TiB_2 nanoparticle agglomeration, resulting in a slight increase in wear rate and a slight rise in COF to 1.96×10^{-6} mm^3/Nm and 0.453, respectively. The aggregation of TiB_2 nanoparticles during HIP treatment led to microstructural inhomogeneity, which caused crack formation and debris generation, ultimately increasing the wear rate. These results indicate that while HIP treatment improved density and eliminated significant porosity, nanoparticle agglomeration compromised the wear resistance, leading to higher wear rates compared to the untreated nanocomposite, as shown in Figure 20d. Hence, post-heat treatment, including the method and the associated processing parameters, should be deliberately identified for improving wear resistance, as it is crucial for the evolution of microstructures. Maintaining the refined microstructures of the as-built state while reducing printing defects should be the key, which shows similarities with the optimization of other properties, such as tensile and fatigue properties.

In summary, enhancing the wear resistance of AM austenitic steels involves modifying their inherent cellular substructure via reinforcement-induced phenomena: solute segregation (CNTs), dislocation pinning (TiC), or in situ fragmentation (SiC). These modifications stabilize the structure against deformation, promoting the formation of a strain-hardened tribolayer. The effectiveness of this approach is inherently tied to the stability window of the dislocation cell structure (typically <600 °C). Beyond this, conventional wear mechanisms re-emerge, indicating that for very high-temperature wear applications, alternative matrix systems or stabilization strategies must be considered.

3.5. Critical Synthesis on the Wear Performance

The preceding survey on the wear properties of AM MMCs across different material systems reveals significant improvements over their unreinforced counterparts, primarily attributed to the incorporation of hard ceramic phases. To advance beyond empirical reporting towards a predictive understanding, a critical synthesis must extract the common principles and matrix-specific strategies governing wear enhancement. The following analysis consolidates these trends through a comparative framework, elucidating the interplay between reinforcement functionality and AM-enabled microstructural control.

The synthesis in Table 2 reveals a universal objective across systems: to engineer a shift from severe to mild wear regimes. However, the pathways to achieve this diverge based on matrix properties and AM process kinetics. In Al- and steel-based systems, the primary strategy is microstructural hardening and stabilization. For Al composites, this is achieved through the uniform dispersion of hard nanoparticles (e.g., TiC), which directly resist abrasion and transition the mechanism from adhesive delamination to controlled abrasive wear. In steel, the inherent dislocation cell structure—a metastable feature of AM—is leveraged and further stabilized by reinforcements (e.g., CNTs inducing carbon segregation), transforming it into a durable, strain-hardened tribolayer.

In contrast, Ti- and Ni-based systems exploit the high-energy AM environment to create novel, in situ functional architectures. For Ti composites, reinforcements like TiC participate in complex dissolution–precipitation cycles, leading not only to grain refinement

but also to the formation of nano-eutectic structures and carbon-enriched solid lubricant films that drastically lower friction. Simultaneously, TiB forms interconnected whisker networks for direct load support. Ni-based systems take this a step further through deliberate in situ phase transformations; reinforcements like WC or ZrB_2 decompose, releasing elements that form nano-dispersed complex carbides and borides within the matrix. This creates a dual benefit: precipitation strengthening of the bulk and the formation of a wear-resistant surface microstructure.

Table 2. Comparative analysis of wear performance mechanisms in AM metal matrix composite systems.

Matrix System	Al-Based	Ti-Based	Ni-Based	Steel-Based
Typical Reinforcements	SiC, TiC (nano)	TiB, TiC	TiC, WC (hybrid)	TiC, CNTs, SiC
Dominant Wear Mechanism Shift	Adhesive to abrasive/oxidative wear	Abrasive/adhesive to surface-protective wear	Severe adhesive to mild abrasive wear	Abrasive/adhesive to strain-hardened layer wear
Key Microstructural Modifier	Uniform nanoparticle dispersion	In situ-formed solid lubricant and reinforcement network	Densification-induced grain refinement and in situ precipitates	Dislocation cell stabilization and reinforcement fragmentation

A critical insight from this comparative analysis is that all these beneficial mechanisms are strictly conditional upon achieving near-full densification and optimal microstructural dispersion. The narrow window for success highlights that AM process parameters are fundamental design variables for wear performance, not mere manufacturing settings. Sub-optimal energy density leads to defects (porosity, unmelted particles) that instantly become sites for crack initiation and catastrophic wear, negating any reinforcement benefit. This intrinsic process–property linkage is even more pronounced for wear than for tensile properties.

This dependency also underscores a major obstacle for the field: the profound lack of standardized wear testing protocols. Direct comparison between studies, as attempted broadly in Figure 10, is severely hampered by variations in applied load, sliding speed, counter face material, and environment. The performance of a composite rated "excellent" under one set of conditions may be mediocre under another. Therefore, the reported mechanisms—while valid within their specific experimental context—require validation across standardized conditions to build universally predictive models. In conclusion, while the literature successfully demonstrates the feasibility of enhancing wear resistance via AM MMCs, a truly critical assessment reveals that the field still heavily relies on phenomenological correlations. To progress, future work must strive to decouple and quantitatively model the contributions of reinforcement characteristics, matrix AM microstructure, and tribologically formed layers under standardized testing conditions.

Furthermore, the matrix-specificity of reinforcement efficacy established for tensile properties holds true for wear. TiB_2 excels in both strength and wear resistance in Al matrices, but through different mechanisms (grain refinement vs. abrasion resistance). The decomposition of ZrB_2 in Ni alloys, beneficial for high-temperature strength via precipitation, also enhances wear resistance by creating a hardened, crack-resistant surface. This underscores that the design of an AM MMC for extreme multifaceted service must be holistic, with reinforcement selection and process optimization simultaneously addressing the intertwined demands of mechanical integrity and surface degradation resistance. Future research must therefore pivot from isolated property enhancement to the integrated, system-level design of materials where microstructural features are tailored to confer synergistic resistance against coupled failure modes.

4. Future Outlook and Challenges

The reviewed studies underscore the significant potential of additive-manufactured metal matrix composites (AM MMCs) to meet the demanding requirements of complex extreme service environments, offering a pathway to synergistic enhancements in strength, toughness, and wear resistance. Despite these promising advancements, the widespread industrial adoption and reliable deployment of AM MMCs are impeded by several persistent challenges. A primary bottleneck lies in controlling process-induced defects and anisotropies. The complex, non-equilibrium thermal cycles inherent to AM can lead to inconsistent microstructures, resulting in material anisotropy and defects such as porosity and lack of fusion, which compromise mechanical reliability and demand precise parameter optimization coupled with advanced in situ monitoring. Furthermore, the development of these materials remains largely empirical due to a limited predictive capability. The absence of robust, multi-scale models that quantitatively link powder composition, AM process parameters, as-built microstructure, and ultimate performance necessitates a slow, trial-and-error approach. The field also grapples with a lack of standardized material and process protocols. The variability in powder feedstock characteristics, along with undefined optimal process parameters and qualification methods, creates significant hurdles for the certification and integration of AM MMCs into mission-critical applications. Finally, economic and scalability barriers related to the cost of specialized composite powders and the relatively low build rates of some AM technologies must be overcome to enable cost-competitive large-scale production.

To address these bottlenecks and fully realize the transformative potential of AM MMCs, future research and development must converge on several key frontiers: The shift from empirical methods to knowledge-driven, predictive design via Integrated Computational Materials Engineering (ICME) and Artificial Intelligence (AI) is paramount. This requires developing hierarchical computational frameworks that integrate simulations of melt pool dynamics, solidification, and mesoscale mechanical response with machine learning to enable the inverse design of materials and processes for target properties. Secondly, leveraging AM's unique spatial control to move beyond homogeneous composites towards intelligent, graded, and multi-functional architectures is essential. This includes the fabrication of functionally graded materials (FGMs) with tailored reinforcement distributions, the hybrid manufacturing of multi-material components, and the design of bio-inspired lattice structures. Lastly, ensuring consistency and reliability necessitates a holistic approach towards full-process digitalization and the establishment of digital twins. This involves implementing in-process monitoring with real-time closed-loop control, developing tailored post-processing treatments for AM-specific microstructures, and constructing component-level digital models that integrate as-built defect data with service load simulations to predict remaining useful life, thereby forming the basis for predictive maintenance strategies.

5. Conclusions

Based on a comprehensive review of the mechanical and wear properties of AM MMCs for extreme service environments, the following principal conclusions can be drawn:

1. Synergistic property enhancement is achievable via AM. The integration of carefully selected ceramic reinforcements (e.g., TiB_2, TiC) with the unique rapid solidification kinetics of AM enables a concurrent improvement in high-temperature strength and wear resistance, moving beyond single-property optimization. For instance, yield strengths exceeding 900 MPa have been realized in Al matrix composites with TiC reinforcement, while specific wear rates have been reduced by an order of magnitude (e.g., to ~2.76×10^{-5} mm^3/Nm) in TiC/AlSi10Mg systems. This synergy stems

from the multi-functional role of uniformly dispersed reinforcements, which provide grain refinement via heterogeneous nucleation, stabilize microstructure through Zener pinning at elevated temperatures (e.g., retaining strength up to 300–500 °C in various systems), and act as direct load-bearing phases to resist abrasive and adhesive wear.

2. The "process–structure–property" relationship is paramount. Performance is critically governed by AM process parameters, which dictate melt pool dynamics and solidification rates, thereby controlling reinforcement distribution, interfacial integrity, and matrix substructure (e.g., dislocation cells with spacing often below 1 μm). Achieving near-full density (>98%) and a uniform, refined microstructure is a prerequisite for optimal properties. However, this also introduces inherent anisotropy and a delicate balance where reinforcement can both mitigate (by disrupting columnar grains) and exacerbate (by acting as stress concentrators) the defects and directional characteristics inherited from the AM process.
3. Degradation in complex service involves coupled mechanisms. Material performance under extreme conditions is governed by nonlinear interactions between mechanical and tribological degradation pathways. For example, high-temperature softening can accelerate wear rates, while wear-induced surface damage and microcracks can become initiation sites for fatigue or creep failure, reducing the effective load-bearing cross-section. This interdependence underscores the necessity for an integrated, system-level evaluation framework for AM MMCs, rather than isolated property assessment.
4. Reinforcement efficacy is highly matrix-specific. TiB_2 and TiC excel in Al and Ni matrices due to favorable interfacial stability and grain refinement, whereas in Ti alloys, in situ-formed TiB whiskers are superior. Conversely, some reinforcements like SiC can degrade performance in certain AM processes due to deleterious interfacial reactions. The selection must therefore be tailored based on thermodynamic compatibility with the matrix and the target service temperature window.
5. Wear resistance is dictated by a triad of factors. Enhanced wear performance (often evidenced by friction coefficient reductions from ~0.6 to ~0.3–0.4) arises from the interplay of the following: (i) reinforcement characteristics (hardness, size, distribution), (ii) the native AM matrix microstructure (e.g., stable dislocation cells), and (iii) the formation of protective tribolayers during sliding. Optimal wear resistance is achieved only within a narrow window of reinforcement content (often 2–10 vol%) and AM energy density, beyond which defects or particle agglomeration lead to performance deterioration.

In summary, this review demonstrates that AM presents a transformative pathway for fabricating high-performance MMCs capable of withstanding coupled extreme conditions. By leveraging precise microstructural control, it is possible to design composites that synergistically enhance strength, thermal stability, and wear resistance. The future of this field lies in building upon these foundational principles through predictive multi-scale design and intelligent manufacturing strategies to unlock the full potential of these advanced materials.

Supplementary Materials: The following supporting information can be downloaded at: https://www.mdpi.com/article/10.3390/met16030260/s1, Table S1: Tensile properties of additive manufactured metal matrix composites; Table S2: Coefficient of friction of additive manufactured metal matrix composites.

Author Contributions: H.F.K.: Formal Analysis, Investigation, Resources, Data Curation, Writing—Original Draft, and Visualization; N.X.: Formal Analysis, Investigation, Resources, and Data Curation; Z.L.: Conceptualization, Methodology, Formal Analysis, Writing—Review and Editing, Supervision,

Project Administration, and Funding Acquisition; S.G.: Methodology, Formal Analysis, Investigation, Resources, Data Curation, Validation, Writing—Original Draft, Visualization, Project Administration, and Funding Acquisition. All authors have read and agreed to the published version of the manuscript.

Funding: The research at SJTU is supported by the Fundamental and Interdisciplinary Disciplines Breakthrough Plan of the Ministry of Education of China (Grant No. JYB2025XDXM210), National Natural Science Foundation of China (Grant Nos. 52171142, 52192595, and 52401194), and Shanghai Jiao Tong University 2030 Initiative.

Data Availability Statement: The original contributions presented in this study are included in the article/Supplementary Materials. Further inquiries can be directed to the corresponding authors.

Conflicts of Interest: The authors declare no conflicts of interest.

References

1. Williams, J.C.; Boyer, R.R. Opportunities and Issues in the Application of Titanium Alloys for Aerospace Components. *Metals* **2020**, *10*, 705. [CrossRef]
2. Su, X.; Zhang, P.; Huang, Y. Research Progress of Metal Additive Manufacturing Technology and Application in Space: A Review. *Metals* **2024**, *14*, 1373. [CrossRef]
3. Awang, M.; Khalili, A.A.; Pedapati, S.R. A Review: Thin Protective Coating for Wear Protection in High-Temperature Application. *Metals* **2019**, *10*, 42. [CrossRef]
4. Torres, H.; Varga, M.; Adam, K.; Rodríguez Ripoll, M. The role of load on wear mechanisms in high temperature sliding contacts. *Wear* **2016**, *364–365*, 73–83. [CrossRef]
5. Zhong, W.; Hu, J.J.; Shen, P.; Wang, C.Y.; Lius, Q.Y. Experimental investigation between rolling contact fatigue and wear of high-speed and heavy-haul railway and selection of rail material. *Wear* **2011**, *271*, 2485–2493. [CrossRef]
6. Ren, C.; Chen, K.; Liang, J.; Narayan, R.L.; Ramamurty, U.; Li, J. Microstructural evolution and its influence on the wear resistance of a laser directed energy deposited Ni-based single crystal superalloy. *J. Mater. Sci. Technol.* **2025**, *205*, 127–138. [CrossRef]
7. Halchak, J.A.; Cannon, J.L.; Brown, C. *Materials for Liquid Propulsion Systems*; American Institute of Aeronautics and Astronautics: Reston, VA, USA, 2018.
8. Sharma, D.K.; Mahant, D.; Upadhyay, G. Manufacturing of metal matrix composites: A state of review. *Mater. Today Proc.* **2020**, *26*, 506–519. [CrossRef]
9. Suryanarayana, C. Mechanical alloying and milling. *Prog. Mater. Sci.* **2001**, *46*, 1–184. [CrossRef]
10. Saini, H.; Khatri, M.S. A Topical Review on Electrodeposited Metal Matrix Nanocomposite Coatings. *J. Electron. Mater.* **2025**, *54*, 6069–6095. [CrossRef]
11. Wang, Z.; Gao, S.; Li, S.; Zhang, W.; Lan, L.; Jiang, Y.; He, B. Research progress of laser additive manufacturing nickel-based alloy metal matrix composites. *Metals* **2023**, *13*, 129. [CrossRef]
12. Kotadia, H.R.; Gibbons, G.; Das, A.; Howes, P.D. A review of Laser Powder Bed Fusion Additive Manufacturing of aluminium alloys: Microstructure and properties. *Addit. Manuf.* **2021**, *46*, 102155. [CrossRef]
13. Shi, J.; Wang, Y. Development of metal matrix composites by laser-assisted additive manufacturing technologies: A review. *J. Mater. Sci.* **2020**, *55*, 9883–9917. [CrossRef]
14. Zhang, D.; Qiu, D.; Gibson, M.A.; Zheng, Y.; Fraser, H.L.; St. John, D.H.; Easton, M.A. Additive manufacturing of ultrafine-grained high-strength titanium alloys. *Nature* **2019**, *576*, 91–95. [CrossRef]
15. Wang, G.; Zhang, Y.; Zou, B.; Liu, Y.; Zheng, S.; Li, X.; Yan, W.; Li, Z.; Wang, Y.M. Enhanced plasticity due to melt pool flow induced uniform dispersion of reinforcing particles in additively manufactured metallic composites. *Int. J. Plast.* **2023**, *164*, 103591. [CrossRef]
16. Paoletti, I. Mass Customization with Additive Manufacturing: New Perspectives for Multi Performative Building Components in Architecture. *Procedia Eng.* **2017**, *180*, 1150–1159. [CrossRef]
17. Gu, D.; Shi, X.; Poprawe, R.; Bourell, D.L.; Setchi, R.; Zhu, J. Material-structure-performance integrated laser-metal additive manufacturing. *Science* **2021**, *372*, eabg1487. [CrossRef] [PubMed]
18. Ibrahim, I.A.; Mohamed, F.A.; Lavernia, E.J. Particulate reinforced metal matrix composites—A review. *J. Mater. Sci.* **1991**, *26*, 1137–1156. [CrossRef]
19. Liu, X.; Zhu, J.; He, Y.; Jia, H.; Li, B.; Fang, G. State-of-the-Art Review of the Simulation of Dynamic Recrystallization. *Metals* **2024**, *14*, 1230. [CrossRef]
20. Yang, M.; Wang, L.; Yan, W. Phase-field modeling of grain evolution in additive manufacturing with addition of reinforcing particles. *Addit. Manuf.* **2021**, *47*, 102286. [CrossRef]

21. Rong, X.; Zhao, D.; He, C.; Zhao, N. recent progress in aluminum matrix composites reinforced by in situ oxide ceramics. *J. Mater. Sci.* **2024**, *59*, 9657–9684. [CrossRef]
22. Belelli, F.; Casati, R.; Riccio, M.; Rizzi, A.; Kayacan, M.Y.; Vedani, M. Development of a novel high-temperature Al alloy for laser powder bed fusion. *Metals* **2020**, *11*, 35. [CrossRef]
23. Grzesiak, D.; AlMangour, B.; Krawczyk, M.; Baek, M.S.; Lee, K.A. Selective laser melting of TiC reinforced stainless steel nanocomposites: Mechanical behaviour at elevated temperatures. *Mater Lett.* **2019**, *256*, 126633. [CrossRef]
24. Guo, C.; Yu, Z.; Hu, X.; Li, G.; Zhou, F.; Xu, Z.; Han, S.; Zhou, Y.; Ward, R.M.; Zhu, Q. Y_2O_3 nanoparticles decorated IN738LC superalloy manufactured by laser powder bed fusion: Cracking inhibition, microstructures and mechanical properties. *Compos. Part B* **2022**, *230*, 109555. [CrossRef]
25. He, P.; Kong, H.; Liu, Q.; Ferry, M.; Kruzic, J.J.; Li, X. Elevated temperature mechanical properties of TiCN reinforced AlSi10Mg fabricated by laser powder bed fusion additive manufacturing. *Mater. Sci. Eng. A* **2021**, *811*, 141025. [CrossRef]
26. Li, G.; Huang, Y.; Li, X.; Guo, C.; Zhu, Q.; Lu, J. Laser powder bed fusion of nano-titania modified 2219 aluminium alloy with superior mechanical properties at both room and elevated temperatures: The significant impact of solute. *Addit. Manuf.* **2022**, *60*, 103296. [CrossRef]
27. Li, S.; Li, S.; Liu, H.; Liu, L.; Pan, D.; Li, G.; Wang, Z.; Hou, X.; Gao, J.; Zhang, X. Achieving back-stress strengthening at high temperature via heterogeneous distribution of nano TiBw in titanium alloy by electron beam powder bed fusion. *Mater. Charact.* **2024**, *215*, 114132. [CrossRef]
28. Lin, T.-C.; Cao, C.; Sokoluk, M.; Jiang, L.; Wang, X.; Schoenung, J.M.; Lavernia, E.J.; Li, X. Aluminum with dispersed nanoparticles by laser additive manufacturing. *Nat. Commun.* **2019**, *10*, 4124. [CrossRef]
29. Ma, S.; Dai, J.; Zhang, C.; Wang, M.; Liu, J.; Wang, L.; Wang, H.; Chen, Z. Enhanced high temperature mechanical properties and heat resistance of an Al–Cu–Mg–Fe–Ni matrix composite reinforced with in-situ TiB_2 particles. *J. Mater. Sci.* **2023**, *58*, 13019–13039. [CrossRef]
30. Song, Q.S.; Zhang, Y.; Wei, Y.F.; Zhou, X.Y.; Shen, Y.F.; Zhou, Y.M.; Feng, X.M. Microstructure and mechanical performance of ODS superalloys manufactured by selective laser melting. *Opt. Laser Technol.* **2021**, *144*, 107423. [CrossRef]
31. Song, X.Y.; Shu, S.L.; Zhang, S.; Yang, H.Y.; Qiu, F.; Jiang, Q.C. Microstructure, solidification defects and mechanical properties of high-modulus and high-strength SiC/AlSi10Mg composites fabricated by selective laser melting. *Ceram. Int.* **2024**, *50*, 26607–26623. [CrossRef]
32. Stegman, B.; Yang, B.; Shang, Z.; Ding, J.; Sun, T.; Lopez, J.; Jarosinski, W.; Wang, H.; Zhang, X. Reactive introduction of oxide nanoparticles in additively manufactured 718 Ni alloys with improved high temperature performance. *J. Alloys Compd.* **2022**, *920*, 165846. [CrossRef]
33. Tekoglu, E.; Bae, J.-S.; Kim, H.-A.; Lim, K.-H.; Liu, J.; Doležal, T.D.; Kim, S.Y.; Alrizqi, M.A.; Penn, A.; Chen, W. Superior high-temperature mechanical properties and microstructural features of LPBF-printed In625-based metal matrix composites. *Mater. Today* **2024**, *80*, 297–307. [CrossRef]
34. Tekoğlu, E.; O'Brien, A.D.; Bae, J.-S.; Lim, K.-H.; Liu, J.; Kavak, S.; Ağaoğulları, D.; Chen, W. Metal matrix composite with superior ductility at 800 °C: 3D printed In718+ZrB_2 by laser powder bed fusion. *Compos. Part B* **2024**, *268*, 111052. [CrossRef]
35. Wang, C.; Xiao, Y.; Mi, G.; Zhang, M.; Hua, Z.; Hu, Y. Ti_3SiC_2 reinforced Inconel 625 composites prepared via laser directed energy deposition: New insights into microstructure evolution and mechanical properties. *J. Alloys Compd.* **2024**, *970*, 172396. [CrossRef]
36. Zhang, Z.; Han, Q.; Liu, Z.; Gao, J.; Wang, L.; Liu, H.; Wang, R.; Ma, T.; Gao, Z. Combined effects of heat treatment and TiB_2 content on the high-temperature tensile performance of TiB_2-modified Ni-based GH3230 alloy processed by laser powder bed fusion. *Mater. Sci. Eng. A* **2022**, *861*, 144379. [CrossRef]
37. Zhang, Z.; Han, Q.; Liu, Z.; Wang, X.; Wang, L.; Yang, X.; Ma, T.; Gao, Z. Influence of the TiB_2 content on the processability, microstructure and high-temperature tensile performance of a Ni-based superalloy by laser powder bed fusion. *J. Alloys Compd.* **2022**, *908*, 164656. [CrossRef]
38. Zhang, Z.; Wang, R.; Lv, Y.; Liu, W.; Liu, Y. Microstructures and mechanical properties of heat treated TiC/GTD222 nickel-based composite prepared by selective laser melting. *Mater. Sci. Eng. A* **2022**, *851*, 143588. [CrossRef]
39. Zhao, M.; Song, J.; Tang, Q.; Zhang, Z.; Feng, Q.; Han, Q.; Nie, Y.; Jin, P.; Jin, M.; Wu, H. Laser powder bed fusion of Inconel 718-based composites: Effect of TiB_2 content on microstructure and mechanical performance. *Opt. Laser Technol.* **2023**, *167*, 109596. [CrossRef]
40. Zhong, Y.; Liu, L.; Wikman, S.; Cui, D.; Shen, Z. Intragranular cellular segregation network structure strengthening 316L stainless steel prepared by selective laser melting. *J. Nucl. Mater.* **2016**, *470*, 170–178. [CrossRef]
41. Zhou, Z.; Liu, Y.; Liu, X.; Wu, L. High-temperature tensile and creep properties of TiB-reinforced Ti6Al4V composite fabricated by laser powder bed fusion. *Mater. Charact.* **2023**, *200*, 112859. [CrossRef]
42. Wu, X.; Zhang, W. A review on aluminum matrix composites' characteristics and applications for automotive sector. *Heliyon* **2024**, *10*, e38576. [CrossRef]

43. Kar, A.; Sharma, A.; Kumar, S. A critical review on recent advancements in aluminium-based metal matrix composites. *Crystals* **2024**, *14*, 412. [CrossRef]
44. Rajaram, G.; Kumaran, S.; Rao, T.S. High temperature tensile and wear behaviour of aluminum silicon alloy. *Mater. Sci. Eng. A* **2010**, *528*, 247–253. [CrossRef]
45. Wang, F.; Zeng, J.; Zhang, Y.; Xue, Y. Thermal-mechanical response and load-bearing capacity of large-span linings exposed to high temperatures. *J. Constr. Steel Res.* **2025**, *226*, 109248. [CrossRef]
46. Buha, J.; Lumley, R.; Crosky, A.; Hono, K. Secondary precipitation in an Al–Mg–Si–Cu alloy. *Acta Mater.* **2007**, *55*, 3015–3024. [CrossRef]
47. Devaraj, A.; Wang, W.; Vemuri, R.; Kovarik, L.; Jiang, X.; Bowden, M.; Trelewicz, J.; Mathaudhu, S.; Rohatgi, A. Grain boundary segregation and intermetallic precipitation in coarsening resistant nanocrystalline aluminum alloys. *Acta Mater.* **2019**, *165*, 698–708. [CrossRef]
48. Tjong, S.C. Processing and deformation characteristics of metals reinforced with ceramic nanoparticles. In *Nanocrystalline Materials*; Elsevier: Amsterdam, The Netherlands, 2014; pp. 269–304.
49. Raj Mohan, R.; Venkatraman, R.; Raghuraman, S.; Kumar, P.M.; Rinawa, M.L.; Subbiah, R.; Arulmurugan, B.; Rajkumar, S. Processing of Aluminium-Silicon Alloy with Metal Carbide as Reinforcement through Powder-Based Additive Manufacturing: A Critical Study. *Scanning* **2022**, *2022*, 5610333. [CrossRef]
50. Minasyan, T.; Hussainova, I. Laser powder-bed fusion of ceramic particulate reinforced aluminum alloys: A review. *Materials* **2022**, *15*, 2467. [CrossRef]
51. James, J.; Annamalai, A.R.; Muthuchamy, A.; Jen, C.-P. Effect of wettability and uniform distribution of reinforcement particle on mechanical property (tensile) in aluminum metal matrix composite—A review. *Nanomaterials* **2021**, *11*, 2230. [CrossRef]
52. Wang, P.; Eckert, J.; Prashanth, K.G.; Wu, M.W.; Kaban, I.; Xi, L.X.; Scudino, S. A review of particulate-reinforced aluminum matrix composites fabricated by selective laser melting. *Trans. Nonferrous Met. Soc. China* **2020**, *30*, 2001–2034. [CrossRef]
53. Thümmler, F.; Oberacker, R. *An Introduction to Powder Metallurgy*; CRC Press: Boca Raton, FL, USA, 2024.
54. Zhang, X.; Zheng, H.; Yu, W. A review on solidification cracks in high-strength aluminum alloys via laser powder bed fusion. *Mater. Today Proc.* **2022**, *70*, 465–469. [CrossRef]
55. Nie, J.; Liu, Y.; Wang, F.; Zhou, H.; Cao, Y.; Liu, X.; An, X.; Liao, X.; Zhu, Y.; Zhao, Y. Key roles of particles in grain refinement and material strengthening for an aluminum matrix composite. *Mater. Sci. Eng. A* **2021**, *801*, 140414. [CrossRef]
56. Yuan, P.; Gu, D.; Dai, D. Particulate migration behavior and its mechanism during selective laser melting of TiC reinforced Al matrix nanocomposites. *Mater. Des.* **2015**, *82*, 46–55. [CrossRef]
57. Wang, Z.; Ummethala, R.; Singh, N.; Tang, S.; Suryanarayana, C.; Eckert, J.; Prashanth, K.G. Selective laser melting of aluminum and its alloys. *Materials* **2020**, *13*, 4564. [CrossRef] [PubMed]
58. Dixit, S.; Liu, S. Laser additive manufacturing of high-strength aluminum alloys: Challenges and strategies. *J. Manuf. Mater. Process* **2022**, *6*, 156. [CrossRef]
59. Wang, Q.; Lin, X.; Kang, N.; Wen, X.; Cao, Y.; Lu, J.; Peng, D.; Bai, J.; Zhou, Y.; El Mansori, M. Effect of laser additive manufacturing on the microstructure and mechanical properties of TiB_2 reinforced Al-Cu matrix composite. *Mater. Sci. Eng. A* **2022**, *840*, 142950. [CrossRef]
60. Hao, W.; Ma, S.; Dong, Z.; Hu, Y.; Wang, L.; Chen, H.; Xu, Q.; Dong, H. Atomic characteristics of heterogeneous nucleation during solidification of aluminum alloys: A critical review. *Mater. Genome Eng. Adv.* **2025**, *3*, e65. [CrossRef]
61. Ma, S.; Li, Y.; Kan, W.; Zhang, J.; Wang, M.; Wang, L.; Wu, Y.; Wang, H.; Chen, Z. Enhancement of grain refinement and heat resistance in TiB_2-reinforced Al-Cu-Mg-Fe-Ni matrix composite additive manufactured by electron beam melting. *J. Alloys Compd.* **2022**, *924*, 166395. [CrossRef]
62. Keerthipalli, T.; Aepuru, R.; Biswas, A. Review on precipitation, intermetallic and strengthening of aluminum alloys. *Proc. Inst. Mech. Eng. Part B J. Eng. Manuf.* **2023**, *237*, 833–850. [CrossRef]
63. Sims, Z.C.; Rios, O.R.; Weiss, D.; Turchi, P.E.; Perron, A.; Lee, J.R.; Li, T.T.; Hammons, J.A.; Bagge-Hansen, M.; Willey, T.M. High performance aluminum–cerium alloys for high-temperature applications. *Mater. Horiz.* **2017**, *4*, 1070–1078. [CrossRef]
64. Ballo, P.; Kioussis, N.; Lu, G. Grain boundary sliding and migration: Effect of temperature and vacancies. *Phys. Rev. B* **2001**, *64*, 024104. [CrossRef]
65. O'Brien, C.; Foiles, S. Exploration of the mechanisms of temperature-dependent grain boundary mobility: Search for the common origin of ultrafast grain boundary motion. *J. Mater. Sci.* **2016**, *51*, 6607–6623. [CrossRef]
66. Subramanian, P.; Corderman, R.R.; Amancherla, S.; Oruganti, R.; Angeliu, T.M.; Huang, S.C.; Sanyal, S.; Srinivasan, D.; Anand, K.; Larsen, M. Development of Nanostructured and Nanoparticle Dispersion-Reinforced Metallic Systems-Progress and Challenges. In *Metallic Materials with High Structural Efficiency*; Springer: Dordrecht, The Netherlands, 2004; pp. 55–66.
67. Geng, J.; Hong, T.; Shen, Y.; Liu, G.; Xia, C.; Chen, D.; Wang, M.; Wang, H. Microstructural stability of in-situ TiB_2/Al composite during solution treatment. *Mater. Charact.* **2017**, *124*, 50–57. [CrossRef]

68. Yang, Y.; Yao, W.; Zhang, H. Phase constituents and mechanical properties of laser in-situ synthesized TiCN/TiN composite coating on Ti-6Al-4V. *Surf. Coat. Technol.* **2010**, *205*, 620–624. [CrossRef]
69. Zhu, Z.; Hu, Z.; Seet, H.L.; Liu, T.; Liao, W.; Ramamurty, U.; Nai, S.M.L. Recent progress on the additive manufacturing of aluminum alloys and aluminum matrix composites: Microstructure, properties, and applications. *Int. J. Mach. Tools Manuf.* **2023**, *190*, 104047. [CrossRef]
70. Wang, Z.; Zheng, Z.; Fu, M. Aluminum matrix composites: Structural design and microstructure evolution in the deformation process. *J. Mater. Res. Technol.* **2024**, *30*, 3724–3754. [CrossRef]
71. Li, A.; Wang, G.; Zhang, X.; Li, Y.; Gao, X.; Sun, H.; Qian, M.; Cui, X.; Geng, L.; Fan, G. Enhanced combination of strength and ductility in ultrafine-grained aluminum composites reinforced with high content intragranular nanoparticles. *Mater. Sci. Eng. A* **2019**, *745*, 10–19. [CrossRef]
72. Kumar, A.; Singh, V.P.; Singh, R.; Chaudhary, R.; Kumar, D.; Mourad, A.-H.I. A review of aluminum metal matrix composites: Fabrication route, reinforcements, microstructural, mechanical, and corrosion properties. *J. Mater. Sci.* **2024**, *59*, 2644–2711. [CrossRef]
73. Taloni, A.; Vodret, M.; Costantini, G.; Zapperi, S. Size effects on the fracture of microscale and nanoscale materials. *Nat. Rev. Mater.* **2018**, *3*, 211–224. [CrossRef]
74. Su, W.; Wang, H.; Li, G.; Zhang, Y. Evolution of microstructure and mechanical properties of aluminum matrix composites reinforced with dual-phase heterostructures. *Mater. Sci. Eng. A* **2024**, *901*, 146500. [CrossRef]
75. Wan, J.; Geng, H.; Chen, B.; Shen, J.; Kondoh, K.; Li, J. Evading ductility deterioration in aluminum matrix composites via intragranulation of nano-reinforcement by reactive selective laser melting. *Mater. Sci. Eng. A* **2023**, *863*, 144552. [CrossRef]
76. Zou, B.; Wang, L.; Zhang, Y.; Liu, Y.; Ouyang, Q.; Jin, S.; Zhang, D.; Yan, W.; Li, Z. Enhanced strength and ductility of metal composites with intragranularly dispersed reinforcements by additive manufacturing. *Mater. Res. Lett.* **2023**, *11*, 360–366. [CrossRef]
77. Zhu, Y.; Wu, X. Heterostructured materials. *Prog. Mater. Sci.* **2023**, *131*, 101019. [CrossRef]
78. Shahadat, M.; Teng, T.T.; Rafatullah, M.; Arshad, M. Titanium-based nanocomposite materials: A review of recent advances and perspectives. *Colloids Surf. B* **2015**, *126*, 121–137. [CrossRef]
79. Attar, H.; Ehtemam-Haghighi, S.; Kent, D.; Dargusch, M.S. Recent developments and opportunities in additive manufacturing of titanium-based matrix composites: A review. *Int. J. Mach. Tools Manuf.* **2018**, *133*, 85–102. [CrossRef]
80. Liu, Z.; He, B.; Lyu, T.; Zou, Y. A review on additive manufacturing of titanium alloys for aerospace applications: Directed energy deposition and beyond Ti-6Al-4V. *J. Miner. Met. Mater. Soc.* **2021**, *73*, 1804–1818. [CrossRef]
81. Liu, Z.; Xin, S.; Zhao, Y. Research progress on the creep resistance of high-temperature titanium alloys: A review. *Metals* **2023**, *13*, 1975. [CrossRef]
82. Li, Q.; Huang, S.; Zhao, Y.; Gao, Y.; Ramamurty, U. Simultaneous enhancements of strength, ductility, and toughness in a TiB reinforced titanium matrix composite. *Acta Mater.* **2023**, *254*, 118995. [CrossRef]
83. Kumar, P.; Prakash, O.; Ramamurty, U. Micro-and meso-structures and their influence on mechanical properties of selectively laser melted Ti-6Al-4V. *Acta Mater.* **2018**, *154*, 246–260. [CrossRef]
84. Yang, J.; Chang, R.; Gao, P.; Wei, S.; Ji, W.; Lu, Z.; Yao, C.; Xiao, S.; Chen, Y. The creep behavior of (TiB+ TiC+ Y_2O_3)/α-Ti composites at high temperature and short-term. *Mater. Charact.* **2022**, *194*, 112443. [CrossRef]
85. Bała, P.; Górecki, K.; Dziurka, R.; Kozieł, T. The Effect of Al and Ti Additions on Solid Solution Strengthening and Precipitation Hardening in CoNiFe Medium-Entropy Alloys. *Materials* **2023**, *16*, 6297. [CrossRef] [PubMed]
86. Zhang, J.; Bermingham, M.J.; Otte, J.; Liu, Y.; Hou, Z.; Yang, N.; Yin, Y.; Bayat, M.; Lin, W.; Huang, X. Ultrauniform, strong, and ductile 3D-printed titanium alloy through bifunctional alloy design. *Science* **2024**, *383*, 639–645. [CrossRef] [PubMed]
87. Leyens, C.; Peters, M. *Titanium and Titanium Alloys: Fundamentals and Applications*; Wiley Online Library: Hoboken, NJ, USA, 2006.
88. Pouzet, S.; Peyre, P.; Gorny, C.; Castelnau, O.; Baudin, T.; Brisset, F.; Colin, C.; Gadaud, P. Additive layer manufacturing of titanium matrix composites using the direct metal deposition laser process. *Mater. Sci. Eng. A* **2016**, *677*, 171–181. [CrossRef]
89. Kang, L.; Yang, C. A review on high-strength titanium alloys: Microstructure, strengthening, and properties. *Adv. Eng. Mater.* **2019**, *21*, 1801359. [CrossRef]
90. Huang, L.; An, Q.; Geng, L.; Wang, S.; Jiang, S.; Cui, X.; Zhang, R.; Sun, F.; Jiao, Y.; Chen, X. Multiscale architecture and superior high-temperature performance of discontinuously reinforced titanium matrix composites. *Adv. Mater.* **2021**, *33*, 2000688. [CrossRef]
91. Schwaighofer, E.; Rashkova, B.; Clemens, H.; Stark, A.; Mayer, S. Effect of carbon addition on solidification behavior, phase evolution and creep properties of an intermetallic β-stabilized γ-TiAl based alloy. *Intermetallics* **2014**, *46*, 173–184. [CrossRef]
92. Ezugwu, E.; Wang, Z.; Machado, A. The machinability of nickel-based alloys: A review. *J. Mater. Process Technol.* **1999**, *86*, 1–16. [CrossRef]
93. Hamdi, H.; Abedi, H.R. Thermal stability of Ni-based superalloys fabricated through additive manufacturing: A review. *J. Mater. Res. Technol.* **2024**, *30*, 4424–4476. [CrossRef]

94. Shahwaz, M.; Nath, P.; Sen, I. A critical review on the microstructure and mechanical properties correlation of additively manufactured nickel-based superalloys. *J. Alloys Compd.* **2022**, *907*, 164530. [CrossRef]
95. Yu, H.; Hayashi, S.; Kakehi, K.; Kuo, Y.-L. Study of formed oxides in IN718 alloy during the fabrication by selective laser melting and electron beam melting. *Metals* **2018**, *9*, 19. [CrossRef]
96. Tekoğlu, E.; O'Brien, A.D.; Liu, J.; Wang, B.; Kavak, S.; Zhang, Y.; Kim, S.Y.; Wang, S.; Ağaoğulları, D.; Chen, W. Strengthening additively manufactured Inconel 718 through in-situ formation of nanocarbides and silicides. *Addit. Manuf.* **2023**, *67*, 103478. [CrossRef]
97. Li, N.; Liu, W.; Wang, Y.; Zhao, Z.; Yan, T.; Zhang, G.; Xiong, H. Laser additive manufacturing on metal matrix composites: A review. *Chin. J. Mech. Eng.* **2021**, *34*, 38. [CrossRef]
98. Zheng, Y.; Liu, F.; Zhang, W.; Liu, F.; Huang, C.; Gao, J.; Li, Q. The microstructure evolution and precipitation behavior of TiB_2/Inconel 718 composites manufactured by selective laser melting. *J. Manuf. Process* **2022**, *79*, 510–519. [CrossRef]
99. Bramfitt, B.L. The effect of carbide and nitride additions on the heterogeneous nucleation behavior of liquid iron. *Met. Trans.* **1970**, *1*, 1987–1995. [CrossRef]
100. Munro, R.G. Material properties of titanium diboride. *J. Res. Natl. Inst. Stand. Technol.* **2000**, *105*, 709. [CrossRef]
101. Chen, C.; Yin, J.; Zhu, H.; Zeng, X.; Wang, G.; Ke, L.; Zhu, J.; Chang, S. The effect of process parameters on the residual stress of selective laser melted Inconel 718 thin-walled part. *Rapid Prototyp. J.* **2019**, *25*, 1359–1369. [CrossRef]
102. Shu, C.; Chen, S.; Lei, P.; Shu, X.; Abdel-Wahab, A.; Essa, K. Effect and mechanism of powder morphology on mechanical properties of nickel-based metal matrix composites TiC-IN738LC in laser powder bed fusion. *Prog. Addit. Manuf.* **2025**, *10*, 7835–7853. [CrossRef]
103. Hart, E. Theory of the tensile test. *Acta Met.* **1967**, *15*, 351–355. [CrossRef]
104. Tang, Y.T.; Karamched, P.; Liu, J.; Haley, J.C.; Reed, R.C.; Wilkinson, A.J. Grain boundary serration in nickel alloy inconel 600: Quantification and mechanisms. *Acta Mater.* **2019**, *181*, 352–366. [CrossRef]
105. Kontis, P.; Alabort, E.; Barba, D.; Collins, D.M.; Wilkinson, A.J.; Reed, R.C. On the role of boron on improving ductility in a new polycrystalline superalloy. *Acta Mater.* **2017**, *124*, 489–500. [CrossRef]
106. Hong, H.U.; Jeong, H.W.; Kim, I.S.; Choi, B.G.; Yoo, Y.S.; Jo, C.Y. Significant decrease in interfacial energy of grain boundary through serrated grain boundary transition. *Philos. Mag.* **2012**, *92*, 2809–2825. [CrossRef]
107. de Bellefon, G.M.; Van Duysen, J. Tailoring plasticity of austenitic stainless steels for nuclear applications: Review of mechanisms controlling plasticity of austenitic steels below 400 C. *J. Nucl. Mater.* **2016**, *475*, 168–191. [CrossRef]
108. Zhai, W.; Zhou, W.; Zhu, Z.; Nai, S.M.L. Selective laser melting of 304L and 316L stainless steels: A comparative study of microstructures and mechanical properties. *Steel Res. Int.* **2022**, *93*, 2100664. [CrossRef]
109. Deng, P.; Yin, H.; Song, M.; Li, D.; Zheng, Y.; Prorok, B.C.; Lou, X. On the thermal stability of dislocation cellular structures in additively manufactured austenitic stainless steels: Roles of heavy element segregation and stacking fault energy. *J. Miner. Met. Mater. Soc.* **2020**, *72*, 4232–4243. [CrossRef]
110. Bertsch, K.; De Bellefon, G.M.; Kuehl, B.; Thoma, D. Origin of dislocation structures in an additively manufactured austenitic stainless steel 316L. *Acta Mater.* **2020**, *199*, 19–33. [CrossRef]
111. Martin, S.; Wolf, S.; Martin, U.; Krüger, L.; Rafaja, D. Deformation mechanisms in austenitic TRIP/TWIP steel as a function of temperature. *Met. Mater. Trans. A* **2016**, *47*, 49–58. [CrossRef]
112. Li, Y.; Krajňák, T.; Podaný, P.; Veselý, J.; Džugan, J. Thermal stability of dislocation structure and its effect on creep property in austenitic 316L stainless steel manufactured by directed energy deposition. *Mater. Sci. Eng. A* **2023**, *873*, 144981. [CrossRef]
113. Molnar, D.; Sun, X.; Lu, S.; Li, W.; Engberg, G.; Vitos, L. Effect of temperature on the stacking fault energy and deformation behaviour in 316L austenitic stainless steel. *Mater. Sci. Eng. A* **2019**, *759*, 490–497. [CrossRef]
114. Lo, K.H.; Shek, C.H.; Lai, J. Recent developments in stainless steels. *Mater. Sci. Eng. R Rep.* **2009**, *65*, 39–104. [CrossRef]
115. Yan, F.; Liu, G.; Tao, N.; Lu, K. Strength and ductility of 316L austenitic stainless steel strengthened by nano-scale twin bundles. *Acta Mater.* **2012**, *60*, 1059–1071. [CrossRef]
116. AlMangour, B.; Kim, Y.-K.; Grzesiak, D.; Lee, K.-A. Novel TiB_2-reinforced 316L stainless steel nanocomposites with excellent room-and high-temperature yield strength developed by additive manufacturing. *Compos. Part B* **2019**, *156*, 51–63. [CrossRef]
117. Hary, B.; Van Der Meer, M.; Logé, R.; Baudin, T.; de Carlan, Y. Optimization of the thermomechanical treatment to achieve a homogeneous microstructure in a 14cr ODS steel. In Proceedings of the International Conference on Fast Reactors and Related Fuel Cycles Next Generation Nuclear Systems for Sustainable Development (FR17), Iekaterinbourg, Russia, 26–29 June 2017.
118. Wang, C.; Lin, X.; Wang, L.; Zhang, S.; Huang, W. Cryogenic mechanical properties of 316L stainless steel fabricated by selective laser melting. *Mater. Sci. Eng. A* **2021**, *815*, 141317. [CrossRef]
119. Ayers, J.; Schaefer, R.; Robey, W. A laser processing technique for improving the wear resistance of metals. *J. Miner. Met. Mater. Soc.* **1981**, *33*, 19–23. [CrossRef]
120. So, H. The mechanism of oxidational wear. *Wear* **1995**, *184*, 161–167. [CrossRef]

121. Guo, M.; Cao, G.; Pan, H.; Guo, J.; Chen, C.; Zhang, B.; Hu, J. Recent progress in synthesis of MAX phases and oxidation & corrosion mechanism: A review. *Mater. Res. Lett.* **2024**, *12*, 765–796. [CrossRef]
122. Stott, F. The role of oxidation in the wear of alloys. *Tribol. Int.* **1998**, *31*, 61–71. [CrossRef]
123. Ghahremani, A.; Abdullah, A.; Arezoodar, A.F. Wear behavior of metal matrix nanocomposites. *Ceram. Int.* **2022**, *48*, 35947–35965. [CrossRef]
124. Suh, N.P. An overview of the delamination theory of wear. *Wear* **1977**, *44*, 1–16. [CrossRef]
125. Deuis, R.; Subramanian, C.; Yellup, J. Abrasive wear of aluminium composites—A review. *Wear* **1996**, *201*, 132–144. [CrossRef]
126. AlMangour, B.; Grzesiak, D.; Yang, J.-M. Rapid fabrication of bulk-form TiB_2/316L stainless steel nanocomposites with novel reinforcement architecture and improved performance by selective laser melting. *J. Alloys Compd.* **2016**, *680*, 480–493. [CrossRef]
127. AlMangour, B.; Grzesiak, D.; Yang, J.-M. Nanocrystalline TiC-reinforced H13 steel matrix nanocomposites fabricated by selective laser melting. *Mater. Des.* **2016**, *96*, 150–161. [CrossRef]
128. AlMangour, B.; Grzesiak, D.; Yang, J.-M. Selective laser melting of TiB_2/H13 steel nanocomposites: Influence of hot isostatic pressing post-treatment. *J. Mater. Process Technol.* **2017**, *244*, 344–353. [CrossRef]
129. Cai, C.; Radoslaw, C.; Zhang, J.; Yan, Q.; Wen, S.; Song, B.; Shi, Y. In-Situ preparation and formation of TiB/Ti-6Al-4V nanocomposite via laser additive manufacturing: Microstructure evolution and tribological behavior. *Powder Technol.* **2019**, *342*, 73–84. [CrossRef]
130. Chang, F.; Gu, D.; Dai, D.; Yuan, P. Selective laser melting of in-situ Al4SiC4+ SiC hybrid reinforced Al matrix composites: Influence of starting SiC particle size. *Surf. Coat. Technol.* **2015**, *272*, 15–24. [CrossRef]
131. Chen, L.; Sun, Y.; Li, L.; Ren, Y.; Ren, X. In situ TiC/Inconel 625 nanocomposites fabricated by selective laser melting: Densification behavior, microstructure evolution, and wear properties. *Appl. Surf. Sci.* **2020**, *518*, 145981. [CrossRef]
132. Fereiduni, E.; Ghasemi, A.; Elbestawi, M. Microstructural characterization and mechanical properties of nano-scale/sub-micron TiB-reinforced titanium matrix composites fabricated by laser powder bed fusion. *J. Alloys Compd.* **2022**, *896*, 163054. [CrossRef]
133. Gu, D.; Hagedorn, Y.C.; Meiners, W.; Wissenbach, K.; Poprawe, R. Nanocrystalline TiC reinforced Ti matrix bulk-form nanocomposites by Selective Laser Melting (SLM): Densification, growth mechanism and wear behavior. *Compos. Sci. Technol.* **2011**, *71*, 1612–1620. [CrossRef]
134. Gu, D.; Wang, H.; Dai, D.; Chang, F.; Meiners, W.; Hagedorn, Y.-C.; Wissenbach, K.; Kelbassa, I.; Poprawe, R. Densification behavior, microstructure evolution, and wear property of TiC nanoparticle reinforced AlSi10Mg bulk-form nanocomposites prepared by selective laser melting. *J. Laser Appl.* **2014**, *27*, S17003. [CrossRef]
135. Gu, D.; Zhang, H.; Dai, D.; Xia, M.; Hong, C.; Poprawe, R. Laser additive manufacturing of nano-TiC reinforced Ni-based nanocomposites with tailored microstructure and performance. *Compos. Part B Eng.* **2019**, *163*, 585–597. [CrossRef]
136. Jia, Q.; Gu, D. Selective laser melting additive manufacturing of TiC/Inconel 718 bulk-form nanocomposites: Densification, microstructure, and performance. *J. Mater. Res. Technol.* **2014**, *29*, 1960–1969. [CrossRef]
137. Kim, S.H.; Shin, G.H.; Kim, B.K.; Kim, K.T.; Yang, D.Y.; Aranas, C.; Choi, J.P.; Yu, J.H. Thermo-mechanical improvement of Inconel 718 using ex situ boron nitride-reinforced composites processed by laser powder bed fusion. *Sci. Rep.* **2017**, *7*. [CrossRef] [PubMed]
138. Kong, D.; Dong, C.; Ni, X.; Zhang, L.; Man, C.; Zhu, G.; Yao, J.; Wang, L.; Cheng, X.; Li, X. Effect of TiC content on the mechanical and corrosion properties of Inconel 718 alloy fabricated by a high-throughput dual-feed laser metal deposition system. *J. Alloys Compd.* **2019**, *803*, 637–648. [CrossRef]
139. Liu, X.; Shi, X.; Huang, Y.; Deng, X.; Lu, G.; Yan, Z.; Zhou, H.; Xue, B. The sliding wear and friction behavior of M50-graphene self-lubricating composites prepared by laser additive manufacturing at elevated temperature. *J. Mater. Eng. Perform.* **2018**, *27*, 985–996. [CrossRef]
140. Patil, A.S.; Hiwarkar, V.D.; Verma, P.K.; Khatirkar, R.K. Effect of TiB_2 addition on the microstructure and wear resistance of Ti-6Al-4V alloy fabricated through direct metal laser sintering (DMLS). *J. Alloys Compd.* **2019**, *777*, 165–173. [CrossRef]
141. Rong, T.; Gu, D.; Shi, Q.; Cao, S.; Xia, M. Effects of tailored gradient interface on wear properties of WC/Inconel 718 composites using selective laser melting. *Surf. Coat. Technol.* **2016**, *307*, 418–427. [CrossRef]
142. Tang, M.; Zhang, L.; Zhang, N. Microstructural evolution, mechanical and tribological properties of TiC/Ti6Al4V composites with unique microstructure prepared by SLM. *Mater. Sci. Eng. A* **2021**, *814*, 141187. [CrossRef]
143. Xi, X.; Chen, B.; Tan, C.; Song, X.; Feng, J. Microstructure and mechanical properties of SiC reinforced AlSi10Mg composites fabricated by laser metal deposition. *J. Manuf. Process* **2020**, *58*, 763–774. [CrossRef]
144. Yang, Y.; Ma, S.; Liu, G.; Wang, T.; Lei, J. Nano and micron WC particles reinforced Hastelloy C22 coatings manufactured by directed energy deposition. *J. Alloys Compd.* **2024**, *970*, 172540. [CrossRef]
145. Yin, H.; Yang, J.; Zhang, Y.; Crilly, L.; Jackson, R.L.; Lou, X. Carbon nanotube (CNT) reinforced 316L stainless steel composites made by laser powder bed fusion: Microstructure and wear response. *Wear* **2022**, *496*, 204281. [CrossRef]
146. Zhao, X.; Lu, X.; Zuo, H.; Ma, S.; Wang, C.; Li, M.V. TiBw reinforced titanium matrix composites fabricated by selective laser melting: Influence of energy density on microstructure and tribological performance. *Ceram. Int.* **2023**, *49*, 28920–28933. [CrossRef]

147. Zhao, Z.; Li, J.; Bai, P.; Qu, H.; Liang, M.; Liao, H.; Wu, L.; Huo, P.; Liu, H.; Zhang, J. Microstructure and mechanical properties of TiC-reinforced 316L stainless steel composites fabricated using selective laser melting. *Metals* **2019**, *9*, 267. [CrossRef]
148. Zou, Y.; Tan, C.; Qiu, Z.; Ma, W.; Kuang, M.; Zeng, D. Additively manufactured SiC-reinforced stainless steel with excellent strength and wear resistance. *Addit. Manuf.* **2021**, *41*, 101971. [CrossRef]
149. Valizade, N.; Farhat, Z. A review on abrasive wear of aluminum composites: Mechanisms and influencing factors. *J. Compos. Sci.* **2024**, *8*, 149. [CrossRef]
150. Abd-Elaziem, W.; Darwish, M.A.; Hamada, A.; Daoush, W.M. Titanium-Based alloys and composites for orthopedic implants Applications: A comprehensive review. *Mater. Des.* **2024**, *241*, 112850. [CrossRef]
151. Chen, Y.; Zhang, H.; Wang, B.; Huang, J.; Zhou, M.; Wang, L.; Xi, Y.; Jia, H.; Xu, S.; Liu, H. A Review of Research on Improving Wear Resistance of Titanium Alloys. *Coatings* **2024**, *14*, 786. [CrossRef]
152. Bai, H.; Zhong, L.; Kang, L.; Liu, J.; Zhuang, W.; Lv, Z.; Xu, Y. A review on wear-resistant coating with high hardness and high toughness on the surface of titanium alloy. *J. Alloys Compd.* **2021**, *882*, 160645. [CrossRef]
153. PalDey, S.; Deevi, S. Single layer and multilayer wear resistant coatings of (Ti, Al) N: A review. *Mater. Sci. Eng. A* **2003**, *342*, 58–79. [CrossRef]
154. Bian, Y.; Cao, L.; Zeng, D.; Cui, J.; Li, W.; Yu, Z.; Zhang, P. The tribological properties of two-phase hard and soft composite wear-resistant coatings on titanium alloys. *Surf. Coat. Technol.* **2023**, *456*, 129256. [CrossRef]
155. Wang, Y.M.; Voisin, T.; McKeown, J.T.; Ye, J.; Calta, N.P.; Li, Z.; Zeng, Z.; Zhang, Y.; Chen, W.; Roehling, T.T. Additively manufactured hierarchical stainless steels with high strength and ductility. *Nat. Mater.* **2018**, *17*, 63–71. [CrossRef]

Disclaimer/Publisher's Note: The statements, opinions and data contained in all publications are solely those of the individual author(s) and contributor(s) and not of MDPI and/or the editor(s). MDPI and/or the editor(s) disclaim responsibility for any injury to people or property resulting from any ideas, methods, instructions or products referred to in the content.